

Estimation of Sea Spray Aerosol Surface Area over the Southern Ocean Using Scattering Measurements

Moore Kathryn A¹, Alexander Simon Peter², Humphries Ruhi S³, Jensen Jorgen B.⁴, Protat Alain⁵, Reeves Mike⁴, Kreidenweis Sonia M.¹, and DeMott Paul J¹

¹Colorado State University

²Australian Antarctic Division

³CSIRO

⁴National Center for Atmospheric Research (UCAR)

⁵Australian Bureau of Meteorology

November 16, 2022

Abstract

This study focuses on methods to estimate dry marine aerosol surface area (SA) from bulk optical measurements. Aerosol SA is used in many models' ice nucleating particle (INP) parameterizations, as well as influencing particle light scattering, hygroscopic growth, and reactivity, but direct observations are scarce in the Southern Ocean (SO). Two campaigns jointly conducted in austral summer 2018 provided co-located measurements of aerosol surface area from particle size distributions and lidar to evaluate SA estimation methods in this region. Mie theory calculations based on measured size distributions were used to test a proposed approximation for dry aerosol SA, which relies on estimating effective scattering efficiency (Q) as a function of Ångström exponent (\hat{a}). For distributions with dry $\hat{a} < 1$, $Q=2$ was found to be a good approximation within $\pm 50\%$, but for distributions with dry $\hat{a} > 1$, an assumption of $Q=3$ as in some prior studies underestimates dry aerosol surface area by a factor of 2 or more. We propose a new relationship between dry \hat{a} and Q , which can be used for -0.2

Hosted file

essoar.10511336.1.docx available at <https://authorea.com/users/523541/articles/595258-estimation-of-sea-spray-aerosol-surface-area-over-the-southern-ocean-using-scattering-measurements>

Hosted file

cap2_sa_paper_si_kam_final_042522.docx available at <https://authorea.com/users/523541/articles/595258-estimation-of-sea-spray-aerosol-surface-area-over-the-southern-ocean-using-scattering-measurements>

Estimation of Sea Spray Aerosol Surface Area over the Southern Ocean Using Scattering Measurements

Kathryn A. Moore¹, Simon P. Alexander^{2,3}, Ruhi S. Humphries^{4,3}, Jorgen Jensen⁵, Alain Protat^{6,3}, J. Michael Reeves⁵, Sonia M. Kreidenweis¹, and Paul J. DeMott¹

¹Department of Atmospheric Science, Colorado State University, Fort Collins, CO, USA

²Australian Antarctic Division, Hobart, Australia

³Australian Antarctic Programme Partnership, Institute for Marine and Antarctic Science, University of Tasmania, Hobart, Australia

⁴Climate Science Centre, CSIRO Oceans and Atmosphere, Melbourne, Australia

⁵National Center for Atmospheric Research, Boulder, CO, USA

⁶Australian Bureau of Meteorology, Melbourne, Australia

Corresponding author: Kathryn Moore (kathryn.a.moore@colostate.edu)

Key Points:

- Methods to estimate dry marine aerosol surface area from bulk optical measurements were tested for the Southern Ocean region
- A new relationship between effective scattering efficiency and dry Ångström exponent is proposed for nephelometer measurements
- Overestimation of aerosol surface area from previous methods is reduced by derivation of new lidar backscatter conversion parameters

Abstract

This study focuses on methods to estimate dry marine aerosol surface area (SA) from bulk optical measurements. Aerosol SA is used in many models' ice nucleating particle (INP) parameterizations, as well as influencing particle light scattering, hygroscopic growth, and reactivity, but direct observations are scarce in the Southern Ocean (SO). Two campaigns jointly conducted in austral summer 2018 provided co-located measurements of aerosol surface area from particle size distributions and lidar to evaluate SA estimation methods in this region. Mie theory calculations based on measured size distributions were used to test a proposed approximation for dry aerosol SA, which relies on estimating effective scattering efficiency (Q) as a function of Ångström exponent (\AA). For distributions with dry $\text{\AA} < 1$, $Q=2$ was found to be a good approximation within $\pm 50\%$, but for distributions with dry $\text{\AA} > 1$, an assumption of $Q=3$ as in some prior studies underestimates dry aerosol surface area by a factor of 2 or more. We propose a new relationship between dry \AA and Q , which can be used for $-0.2 < \text{\AA} < 2$, and also suggest $\text{\AA}=0.8$ as the cutoff between primary and secondary marine aerosol-dominated distributions. Application of a published methodology to retrieve dry marine aerosol SA from lidar extinction profiles

overestimated aerosol surface area by a factor of 3-5 during these campaigns. Using Microtops aerosol optical thickness measurements, we derive alternative lidar conversion parameters from our observations, applicable to marine aerosol over the Southern Ocean.

Plain Language Summary

The Southern Ocean surrounding Antarctica is one of the few places where aerosol concentrations and composition are similar to pre-industrial values. This makes data collected in this region important for improving and understanding climate model simulations. However, direct observations of aerosols are rare because of the remoteness, frequent storms, and high winds and waves common to the Southern Ocean. In this study, we use some of these rare aerosol observations to test methods for estimating important aerosol quantities using other measurements that are easier to collect. The improvements presented here may increase the availability of key data for improving climate models by replacing rare measurements with ones that can be collected continuously and autonomously.

1. Introduction

The Southern Ocean (SO) is a vast region of water surrounding Antarctica, separating it from the other Southern Hemisphere landmasses. Its remoteness from continental and anthropogenic aerosol sources and persistent strong westerlies help isolate the region, and both in situ observations (Humphries et al., 2021; Mace et al., 2020; Quinn et al., 2017) and modeling studies (Hamilton et al., 2014; McCoy et al., 2015) have indicated that the predominant aerosol sources in the boundary layer are local. As a result, the SO may serve as a proxy for pre-industrial marine aerosol conditions (Hamilton et al., 2014) and is a good location to test aerosol-cloud interactions in models. Aerosols directly influence atmospheric radiative forcing through scattering and absorption of solar radiation, as well as indirectly through aerosol-cloud interactions such as nucleation of cloud droplets and ice crystals. They contribute the largest uncertainty to global radiative forcing estimates, with natural aerosols responsible for a significant portion of this, making observations in areas free of anthropogenic influences, such as the SO, critical (Andreae, 2007; Carslaw et al., 2013; Kiehl, 2007). However, difficulty in reaching the SO, coupled with frequent storms and high winds, have led to a paucity of direct aerosol, cloud, and precipitation observations relative to other regions (McFarquhar et al., 2021).

Aerosols in the SO marine boundary layer (MBL), are primarily of marine origin, and of two types: 1) primary marine aerosol (PMA) generated from sea spray and bubble bursting at the ocean surface and 2) marine biogenic particles that form through condensation of gas-phase species such as dimethyl sulfide (DMS) (Lewis & Schwartz, 2004; Quinn et al., 2017; Sanchez et al., 2021; Twohy et al., 2021). PMA, which is dominated by sea salt, is thought to control the optical properties and direct aerosol radiative forcing in the Southern Ocean (Quinn et al., 1998). Secondary marine biogenic aerosols, which can include sulfur and

carbonaceous components, frequently dominate the cloud condensation nuclei (CCN) budget in the SO MBL, although PMA also contributes significantly to CCN concentrations, particularly under high wind conditions (Fossum et al., 2018; Humphries et al., 2021; Quinn et al., 2017; Sanchez et al., 2021; Twohy et al., 2021). The ice nucleating particle (INP) budget for the SO is not as well constrained as that of CCN, although growing evidence suggests it is also dominated by local marine aerosols (Burrows et al., 2013; McCluskey, Hill, et al., 2018; McFarquhar et al., 2021; Vergara-Temprado et al., 2017).

Low level marine clouds are particularly sensitive to changes in aerosol loading, size, and composition, due to their generally low droplet concentrations. The SO is one of the cloudiest regions on Earth, with low cloud cover (<3 km) approaching or exceeding 80% year round (Mace et al., 2020), and SO clouds are more likely to be supercooled than those at similar temperatures in the Northern Hemisphere (Alexander & Protat, 2018; Chubb et al., 2013; Huang et al., 2012). Despite their prevalence, global climate models (GCMs) struggle to simulate cloud coverage and cloud phase in the region (Kay et al., 2016; McFarquhar et al., 2021). A variety of methods have been used to parametrize ice nucleation in both global and cloud-resolving models, and to compare the relative efficiencies of particle types at nucleating ice. One of the most common methods involves normalizing INP concentrations with a more frequently measured value, such as particle surface area or number (DeMott et al., 2010, 2015; Hoose & Möhler, 2012; Kanji et al., 2017; McCluskey, Ovadnevaite, et al., 2018; Niemand et al., 2012; Ullrich et al., 2017). In addition to use in INP parameterizations, aerosol surface area is an important observational quantity, influencing light scattering, hygroscopic growth, and reactivity (Lewis & Schwartz, 2004; O’Dowd & de Leeuw, 2007).

The need for observations of particle number and surface area concentrations, both to directly compare to modeled values, as well as to evaluate and improve marine INP parameterizations, was the primary motivation for this study. Particularly over the SO, measurements of aerosol size distributions are infrequent and limited in spatial and temporal extent. Estimating aerosol properties using light scattering observations from nephelometers and lidars is appealing because of their autonomous operation and higher availability of measurements. Two techniques for retrieving marine aerosol surface area from bulk optical measurements will be evaluated here for the Southern Ocean. The first, proposed in DeMott et al. (2016), uses ambient aerosol scattering coefficients from a three-channel nephelometer, and the second utilizes lidar aerosol backscatter profiles (Mamouri & Ansmann, 2016), and are described further in Sec. 2.3.4 and 2.2. To our knowledge, neither of these methods have been previously applied to observations from the Southern Ocean marine boundary layer. Two campaigns that occurred concurrently in 2018, the Southern Ocean Cloud Radiation Aerosol Transport Experimental Study (SOCRATES, hereafter SOC) aircraft campaign and the second Clouds, Aerosols, Precipitation, Radiation and atmospheric Composition Over the southeRN ocean (CAPRICORN-2, hereafter CAP-2) ship campaign, provide a unique opportunity to assess these techniques

with co-located aerosol size distribution measurements that were used to validate proposed conversion parameters (Sec. 3.2 and 3.3).

1. Methods

(a) Overview of CAPRICORN-2 and SOCRATES Campaigns

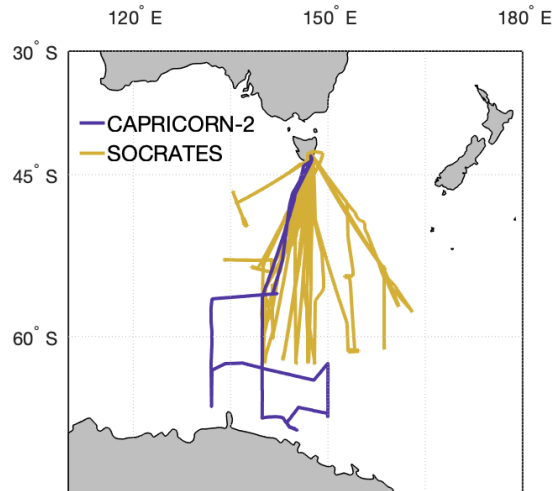


Figure 1. Track of the RV *Investigator* (CAPRICORN-2) and flight tracks from the NSF/NCAR G-V (SOCRATES) are shown in purple and gold, respectively.

The SOC and CAP-2 campaigns occurred simultaneously during January-March 2018 in the Southern Ocean region south of Tasmania with the goal of providing in-situ measurements to improve and validate climate model simulations of marine boundary layer processes, clouds, and aerosols over the Southern Ocean. The SOC campaign used the NSF/NCAR G-V aircraft to make measurements of cloud and aerosol properties in the MBL, within clouds, and above clouds in the region. Complementary MBL measurements were conducted during CAP-2 on the RV *Investigator* (voyage IN2018_V01), an Australian Government research platform operated by the Commonwealth Science and Industrial Research Organisation (CSIRO). Flight tracks for all 15 SOCRATES flights and the ship track for CAPRICORN-2 are shown in Fig. 1. These measurements were made during late austral summer into early austral autumn. Detailed descriptions of the goals, measurements, and preliminary findings for these campaigns are described in

McFarquhar et al. (2021). Coordinated overflights of the ship by the aircraft within the marine boundary layer occurred in a select number of cases, and these will be highlighted in Sec. .

(b) **Use of lidar profiles to estimate aerosol surface area and particle number**

Mamouri and Ansmann (2015, 2016; hereafter MA) proposed a methodology for deriving vertical profiles of dry aerosol surface area, SA_{dry} , and number, N_{dry} , from lidar backscatter profiles and AERONET (Smirnov et al., 2009) observations. Expected uncertainties are in the range 25%-50%. We explored the use of their parameterizations for estimating aerosol surface areas (SAs) and concentrations of particles larger than 500 nm (N_{500}) during CAP-2. Briefly, their methodology involves using Level 2.0 AERONET inversions and correlating surface areas or number concentrations inferred from the inverted volume size distributions with aerosol optical thickness (AOT) at a particular wavelength. The resulting correlations constitute a relationship between column extinction and column aerosol surface area or number, and were derived for three aerosol types: marine, desert dust, and continental (meaning pollution). Lidar ratios representative of the expected aerosol type are used to calculate vertical particle extinction profiles from backscatter data, which are then converted to aerosol SA or N_{500} profiles using the AERONET-extinction relationship for the relevant aerosol type and desired parameter.

To derive a representation appropriate for marine aerosol, which is most relevant for the present study, MA used AERONET data from Ragged Point, Barbados, from 2007-2015, after screening for $AOT_{500 \text{ nm}} < 0.07$ and total Ångström exponent (\AA ; computed for the wavelength pair 440 nm and 870 nm) between 0.25 and 0.6. These criteria removed periods affected by biomass burning emissions and long-range transported dust, which are annual occurrences in the Caribbean region (Corona-Núñez et al., 2020; Prospero et al., 2014). MA derived conversion parameters for three lidar wavelengths: 355 nm, 532 nm, and 1064 nm. A 355-nm lidar was deployed during CAP-2 (Sec.) and this wavelength will be the focus here. Since AERONET measures ambient aerosol, the inverted surface areas and number concentrations must be corrected to dry using an assumed diameter growth factor. For this purpose, a growth factor of 2 was used by MA, corresponding to that expected for sea salt at relative humidities (RH) ~80%, assumed representative of a typical nonprecipitating marine boundary layer. Therefore, wet surface areas were scaled by a factor of 4 to arrive at dry surface areas for marine particles, $SA_{\text{m,dry}}$, assuming no vertical variation in RH :

$$SA_{\text{m,dry}}(z) = \frac{c_{s,m}}{4} \times \sigma_m(z) \#(1)$$

with $SA_{\text{m,dry}}$ in $\text{m}^2 \text{cm}^{-3}$, the conversion factor $c_{s,m}$ in $\text{m}^2 \text{cm}^{-3} \text{Mm}$, and lidar extinction profiles $\sigma_m(z)$ at the applicable wavelength in Mm^{-1} . For a wavelength

of 355 nm, $c_{s,m}/4$ is reported as 0.52 ± 0.09 . To derive dry N_{500} , the AERONET number distributions are integrated for ambient sizes >1000 nm diameter to account for hygroscopic growth:

$$N_{500,m,dry}(z) = c_{1000,m} \times \sigma_m(z) \quad \#(2)$$

with $N_{500,m,dry}$ in cm^{-3} , and the conversion factor $c_{1000,m}$ in $\text{cm}^{-3} \text{ Mm}$; at 355 nm, $c_{1000,m}=0.05\pm 0.01$.

1. Aerosol Measurements during CAPRICORN-2

(a) RV *Investigator* Aerosol Inlet

The aerosol laboratory on the RV *Investigator* contained a suite of instruments for measuring aerosol properties. These included sub- and super-micron aerosol size distributions, aerosol scattering, aerosol chemical composition, cloud condensation nuclei number concentration, fluorescent biological particles, and total aerosol number concentration. The RV *Investigator* has a custom-designed aerosol sampling inlet, with the intake located approximately 18.4 m above sea level at the bow of the ship. The whole inlet is stainless steel, with an inner diameter of 16 cm, which tapers to a 4 cm conical intake. Ambient air is sampled into the conical intake section at $\sim 440 \text{ L min}^{-1}$, which is oriented horizontally to limit the amount of precipitation entering the inlet, and automatically adjusts to orient into the wind (forward 180° only). The inlet then travels vertically down the foremast into the aerosol lab, which is located directly underneath the inlet at the bow of the ship, to minimize particle losses. Inside the aerosol lab, approximately 9 m from the intake, is a sample manifold with instrument pickoffs for aerosol sampling. All aerosol instruments considered in this study were located inside the aerosol lab and sampled from the aerosol sampling manifold. Particle transmission efficiency through the aerosol sampling inlet, including dependence on wind speed and ship motion, has not been fully characterized. Preliminary theoretical calculations of transmission efficiency for all data presented here (Sec.) are shown in Fig. S1 which utilized the von der Weiden et al. (2009) Particle Loss Calculator and Paul Baron's Aerocalc spreadsheet (Brockmann, 2011). These calculations assumed a constant aspiration angle of 0° , and a wind velocity of 10 m s^{-1} , which is the average for the CAPRICORN-2 campaign.

(b) Ship Exhaust Contamination and Continental Aerosols

The largest sources of particle contamination on board the RV *Investigator* are exhaust from diesel combustion from the engines and waste incineration. These waste streams are emitted from separate but co-located flues approximately 50 m aft of the aerosol intake, and at a similar height to the sampling inlet (Humphries et al., 2019).

Following the technique presented in Humphries et al. (2019), a timeseries of predicted exhaust influence on measurements during the CAP-2 voyage was created and used to exclude periods of likely exhaust influence from all data presented here. Based on Alexander and Protat (2019), all aerosol measurements north of 47°S were also excluded from this analysis, as the region close to Tasmania occasionally has contributions from continental aerosols.

(c) Particle Size Distribution Measurements

Submicron and supermicron aerosol size distributions were measured directly using a TSI Scanning Mobility Particle Sizer (TSI, SMPS 3080) for aerosols in the range 15-660 nm and a TSI Aerodynamic Particle Sizer (TSI, APS 3320) for aerosols between 500 nm and 20 μ m. A single-jet impactor was located immediately before the SMPS inlet to remove particles larger than the upper scan size. The SMPS size measurements were calibrated before, after, and at two-week intervals during the voyage against polystyrene latex spheres (PSLs) of known sizes. No adjustments were made to the measured electrical mobility sizes, as they agreed with the known PSL sizes to within ± 5 nm during each calibration. SMPS distributions with total number concentrations $< 50 \text{ cm}^{-3}$, as well as all data at sizes < 25 nm were removed due to poor counting statistics and increased noise, respectively. The APS was located approximately 1 m from the sampling manifold, and the inlet minimized bends to reduce losses of supermicron particles. The APS aerodynamic size measurements were calibrated against PSLs of known size and density ($\rho = 1.05 \text{ g cm}^{-3}$) at weekly intervals during the voyage, as well as before and after the campaign. Both aerosol streams were dried with silica gel diffusion driers prior to measurement to below the efflorescence relative humidity (ERH) of sea salt, $\sim 45\text{-}48\%$ (Tang et al., 1997). For submicron size distribution measurements using the SMPS, particles were additionally dried within the instrument due to the introduction of dry sheath air at a 10:1 ratio to the sample flow, and so were assumed to represent aerosol physical dry diameters without additional corrections. Distributions suspected to be influenced by ship exhaust contamination (Sec.) were removed from further analysis, as were any distributions where the instrument inlet RH exceeded 30%.

The SMPS and APS measurements were merged into continuous size distributions following the removal of ship exhaust and high-RH scans. SMPS distributions were averaged to 30-min resolution to reduce noise, then fitted with 3-4 mode lognormal functions to further reduce scatter at the largest sizes (> 450 nm), as in Khlystov et al. (2004). The SMPS sizes were adjusted for shape factor (χ) following DeCarlo et al. (2004) Eq. 25, using $\chi_{\text{SMPS}} = 1.05$ for particles with $0.025 \text{ nm} < D < 500 \text{ nm}$ (Zieger et al., 2017) and assuming the slip

correction factors cancel, since the adjustment is small. The APS distributions were averaged to the same 30-min resolution, then a size-correction factor was applied to convert the APS sizes from D_a to physical dry diameter, accounting for particle density (ρ_p), shape factor, and hygroscopic growth factor (HGF). An APS diameter correction factor of 0.68 was used, which is based on the density of dry sea salt, $\rho_p=2.2 \text{ g cm}^{-3}$ (Lewis & Schwartz, 2004), shape factor measurements of artificial sea salt particles with $D>500\text{nm}$ (Zieger et al., 2017; $\chi=1.03$), and HGF ~ 1 for sea spray aerosols (SSA) below the ERH. Next, the SMPS and APS distributions were combined using a smoothing spline in the overlap region, and this merged distribution was interpolated onto an even diameter grid with logarithmically spaced bins. Finally, the merged distributions were corrected for expected inlet losses as described in Sec. , and 3-4 lognormal modes were fit to each distribution. The inlet transmission efficiency applicable to the APS was used, since minimal losses ($<5\%$) are expected for particles in the SMPS size range (Fig. S1). The merged distributions were cut off at 5 μm dry diameter; above this, the expected transmission efficiency drops below 40%, making the correction highly uncertain (Fig. S1). In total, merged aerosol size distributions were calculated for 1075 30-min periods during CAP-2; a contour plot of the number distributions is given in Fig. S2. Particle surface area and volume distributions were then calculated for each merged number distribution assuming all particles were spherical, as were the number concentrations of particles larger than 500 nm dry diameter (N_{500}).

(d) **Use of bulk scattering coefficients to estimate aerosol surface area**

DeMott et al. (2016; hereafter D16) proposed a method for retrieving dry marine aerosol surface area from ambient bulk aerosol scattering coefficients (b_{sp}), using a three-channel nephelometer. In the absence of available nephelometer data from CAPRICORN-2, theoretical Mie calculations based on the merged aerosol size distributions were used to assess this technique for retrieving marine aerosol SA. In this study, dry scattering distributions and integrated scattering were estimated for each size distribution at wavelengths corresponding to an Ecotech Aurora 4000 Polar Nephelometer (450 nm, 525 nm, 635 nm), using a refractive index of $n=1.5$ (Tang et al., 1997). Ångström exponents (α) were then calculated for each wavelength pair from the calculated scattering coefficients using:

$$= \frac{-\log\left(\frac{b_{sp}^{\lambda_1}}{b_{sp}^{\lambda_2}}\right)}{\log\left(\frac{\lambda_1}{\lambda_2}\right)} \#(3)$$

where λ_1 and λ_2 refer to different measured wavelengths (Seinfeld & Pandis, 2016). Following the methodology of D16, the blue/red λ was used to assign an average aerosol scattering efficiency, Q , under the assumption that the particles being measured can be characterized as having a single effective scattering size. D16 utilized a step function for Q , where if the ambient red/blue $\lambda > 1$, Q was assigned as 3 (submicron particles dominate scattering), and if $\lambda < 1$, Q was assigned as 2 (supermicron particles dominate scattering) (DeMott et al., 2016; Mulcahy et al., 2009). The same thresholds were applied to the dry scattering measurements from CAP-2, which will be discussed further in Sec. . The integrated aerosol surface area can then be estimated from the blue b_{sp} and the calculated scattering efficiency, which further assumes particle sphericity:

$$SA_{\text{scat}} = 4 \left(\frac{b_{sp}^{450 \text{ nm}}}{Q} \right) \quad \#(4)$$

In D16, the estimated aerosol surface areas were then adjusted for hygroscopic growth using the measured RH and assumed HGF. During CAP-2, the aerosol size distributions were measured dry, and no further adjustments were made. Aerosol surface areas calculated using Mie theory and the D16 estimates of Q were compared to those inferred directly from the number distributions to evaluate this technique for dry marine aerosols in Sec. .

1. Lidar

The MA method of retrieving aerosol surface area and N_{500} from lidar profiles was evaluated for the Southern Ocean using the Leosphere RMAN 510 Raman UV polarization lidar (355 nm) deployed on the RV *Investigator* during CAP-2, which provided profiles of height-resolved backscatter along the voyage track (Alexander & Protat, 2019; McFarquhar et al., 2021). The elastic lidar equation was solved using the Rayleigh returns during clear-sky intervals (Fernald, 1984). Only profiles retrieved at night were retained, due to the improved signal-to-noise ratio and profile-to-profile stability of the lidar’s backscatter signal. Lidar particle linear depolarization ratios were consistently less than 5% throughout CAPRICORN-2, indicating hydrated marine aerosols were the primary aerosol type observed (Alexander & Protat, 2019). The near-surface mixed layer mean lidar ratio ($S=20$ sr) observed during CAP-2 and the preceding CAPRICORN-1 voyage (similar region) was used for all profiles to estimate height-resolved aerosol extinction coefficients from the backscatter measurements (Alexander & Protat, 2019). These were then converted to dry aerosol surface area and N_{500} profiles using the MA marine aerosol conversion factors, as described in Sec. . Since MA assumed a constant HGF of 2, whereas the ambient RH is variable, the influence of the HGF value used to derive dry aerosol surface areas was explored using RH measurements collected on the foremast of the RV *Investigator*, followed by calculating an expected HGF for SSA using the Extended Aerosol Inorganic Model (E-AIM; Clegg et al., 1998, 2021) for each lidar profile.

To enable comparisons between the lidar-derived aerosol surface area and N_{500} and those from in-situ aerosol instruments (Sec.), lidar-derived values at an altitude of 300 m were used, which is the lowest level at which the lidar’s overlap function is essentially unity. To minimize differences in the air masses observed by the in-situ and remote-sensing instruments, only lidar profiles where the boundary layer was well-mixed were considered. Formally, the inversion height, identified by radiosondes launched from the ship, was required to be at least 500 m in altitude to ensure lidar data collection within the well-mixed boundary layer. Additionally, the inversion strength of retained profiles was at least 5 K km^{-1} , and the change in potential temperature between the surface and inversion height was $<4 \text{ K}$. Adjusting these thresholds had minimal effect on the lidar profiles selected, since a well-mixed near-surface layer and strong temperature inversions at the top of the boundary layer are often present during clear-sky conditions over the Southern Ocean (Alexander & Protat, 2019). These thresholds and the other requirements discussed above resulted in the selection of 157 ~ 2 min lidar profiles. Aerosol parameters at 300 m derived from the lidar profiles were averaged to the same 30-min intervals as the merged number distributions (Sec.) to facilitate comparisons between the different estimates, resulting in 17 30-min periods.

1. Radiosondes

Radiosondes were launched from the RV *Investigator* every 3-6 hours during CAPRICORN-2, for a total of 234 successful releases (Vömel & Brown, 2018). Vertical profiles of temperature, humidity, and wind were collected for each launch, up to a median altitude of 17.9 km. We determined the altitude of the temperature inversion at the top of boundary layer as the altitude of the maximum vertical gradient in potential temperature between 250 m and 3000 m (Alexander & Protat, 2019). Since radiosondes were launched regularly throughout the campaign, we assume that the thermodynamic profiles sampled by the radiosondes are comparable spatially and temporally with observations made by the lidar directly above the ship.

2. Microtops II Sun Photometer

A portable Microtops II sun photometer instrument was deployed during CAP-2 as part of the AERONET Maritime Aerosol Network (MAN; Smirnov et al., 2009), and was used to collect Ångström exponent (440-870 nm) and AOT (440, 500, 675, 870 nm) data during clear-sky periods. The AOT measurements at 440 nm were extrapolated to 355 nm to match the lidar wavelength (Sec. 2.3.5). As occasionally several measurements were taken sequentially, any measurements collected within 30-min were averaged, to enable comparison with the CAP-2 merged size distributions (Sec.). If a radiosonde sounding (Sec. 2.4) was available within 6 hours, each Microtops AOT measurement was converted to extinction (Mm^{-1}) using the boundary layer inversion height retrieved from the sonde profiles and assuming particles were well mixed vertically within the MBL.

1. Aerosol Measurements during SOCRATES

Aerosol measurements on the G-V (UCAR/NCAR - Earth Observing Laboratory, 2005) considered here consisted of optical detection of submicron particles using two ultra-high sensitivity aerosol spectrometer (Droplet Measurement Technologies, UHSAS) instruments (0.06 - 1.0 μm particle diameters), optical detection of supermicron particles up to 50 μm using a wing-mounted cloud droplet probe (Droplet Measurement Technologies, CDP; Lance et al., 2010), and physical collection and sizing of impacted supermicron particles (0.7-16 μm dry diameter) using the Giant Nucleus Impactor (GNI; Jensen et al., 2020). One UHSAS instrument was mounted on the wing of the G-V and one sampled in the cabin via a counterflow virtual impactor inlet that was also operated for isokinetic total air sampling (Hartery et al., 2020). We primarily employed data from the wing-mounted UHSAS, CDP, and GNI instruments for this study.

The wing-mounted UHSAS data were considered to represent dry particle distributions. As also discussed by Sanchez et al. (2021), we expected that the use of deicing heaters would lower the relative humidity to which particles were exposed to below 40% in the optical cavity, akin to how the same heaters affected particles in the passive cavity aerosol spectrometer probe (PCASP) measurements discussed by Strapp et al. (1992). Striking in the UHSAS measurements in SOCRATES was an apparent particle mode near 0.6-0.7 μm , as shown in Fig. 2. Sanchez et al. (2021) hypothesized that this feature was a consequence of remnant unevaporated water (a deliquescent mode) on the largest particles sensed by the UHSAS. We have since observed that this mode also appears in the UHSAS distributions measured from the CVI inlet inside the G-V cabin (not shown here), which were also assumed to represent dry measurements by Hartery et al. (2020). This suggests that instead of residual water, the feature is a shattering artifact from the inlets, or, more likely, is related to how marine aerosols are sized by the UHSAS. Recent work (Kupc et al., 2018; Moore et al., 2021) has demonstrated that sea spray aerosols, which are expected to have refractive indices much lower than those of the commonly-used PSL calibration particles, will be undersized by the UHSAS. When combined with lower response sensitivity at sizes above 500 nm, such unexpected features may appear in the UHSAS distribution. This topic requires further study and is not further considered here.

Data from the CDP and GNI were merged with the UHSAS to generate distributions to dry sizes $>10 \mu\text{m}$, in order to capture all surface area and volume modes for primary SSA. The first and last three bins of the UHSAS data, and the first two bins of the CDP data, were omitted from these merged distributions since they have low counting efficiencies, and in the case of the CDP, also large variability in Mie scattering. The GNI data reported here represent spherical-equivalent dry sizes of particles collected on slides during flights. The GNI particle sizing procedure, which involves re-humidification of particles to estimate their dry mass on the basis of their wet size and reference to sea salt data from Tang et al. (1997), is fully described in Jensen et al. (2020). Since

both the UHSAS and GNI data are reported dry, it was necessary to adjust the CDP data for water uptake. The CDP data were considered to represent humidified aerosol sizes, in equilibrium with ambient RH, since it is an open-path instrument. The CDP bin sizes were first corrected following Lance et al. (2010), and then further decreased in size based on hygroscopic growth factors predicted for proxy sea salt particles using E-AIM (Clegg et al., 1998, 2021). Sea salt will dominate particle mass at dry sizes above 1 μm and influences of organics on water uptake should be small. Data from the VCSEL water vapor sensor (SouthWest Sciences, I. (SWS) & UCAR/NCAR-Earth Observing Laboratory, 2008; Zondlo et al., 2010) on the G-V (cabin top-mounted inlet) was used to estimate the appropriate HGF for each CDP size distribution based on the ambient relative humidity. We note that the differences between using E-AIM for adjusting the CDP data to dry size versus the reference data in Jensen et al. (2020) could lead to a difference of no more than 5% in dry size between the CDP and GNI.

Thirty-six periods of level G-V flight in the lower marine boundary layer (150 – 300 m MSL) in SOCRATES, covering latitudes from about 49-61°S, were identified for analyses of aerosol distribution data. For each pass, typically 8-10 minutes, relative humidity and horizontal wind speed were averaged, and total CDP concentrations were examined to assure that there was no cloud contamination. Each merged size distribution was then fit with two or three lognormal modes. The sum of the middle and largest (if needed) modes were considered to represent primary marine aerosol, which is further discussed in Sec. . A gap in data availability was always present between the CDP or GNI data in the supermicron regime and the submicron UHSAS data. For all flights where GNI data were available, it was consistently noted that the CDP and GNI distributions agreed quite closely after adjustments were made to correct the CDP bin sizes.

1. Results

(a) Comparison of SOCRATES and CAPRICORN-2 aerosol measurements

An example aerosol number distribution from SOCRATES RF04 on January 24, 2018, is shown in Fig. 2, which includes the average single-mode PMA fit by Sanchez et al. (2021) using only the G-V wing-mounted UHSAS data, in addition to the PMA fit used in this study. Unlike Sanchez et al. (2021), the peak of the narrow mode $\sim 0.6\text{-}0.7 \mu\text{m}$ in the UHSAS data was ignored during fitting in this study, as including it artificially decreases the mode width and forces the mode size into that range. While there is reasonable agreement between both studies at sizes up to 1 μm , our results indicate inclusion of the CDP and GNI data are necessary to clearly define the significant coarse mode present, which becomes increasingly important for estimating PMA surface area and volume concentrations. A broader PMA distribution is consistent with those reported in the

North Atlantic by Saliba et al. (2019) using a similar fit routine as Sanchez et al. (2021). It also agrees well with the regional Southern Ocean distributions of Hartery et al. (2020) describing “sea spray particles” (defined as the distribution humidified to 80% RH) that were composed by combining SOCRATES G-V cabin-based UHSAS data with particle measurements from a separate ship voyage south of New Zealand. Although only a single PMA mode was required to fit the SOCRATES distribution shown in Fig. 2, similarly to O’Dowd et al. (1997), we found 2 PMA modes often provided a better fit than the single-mode fit that has been used more recently (Hartery et al., 2020; Lewis & Schwartz, 2004; Modini et al., 2015; Saliba et al., 2019; Sanchez et al., 2021). This may be related to the longer, usually hourly, averaging times used by most studies, as compared to the 8-10 min level legs during SOCRATES.

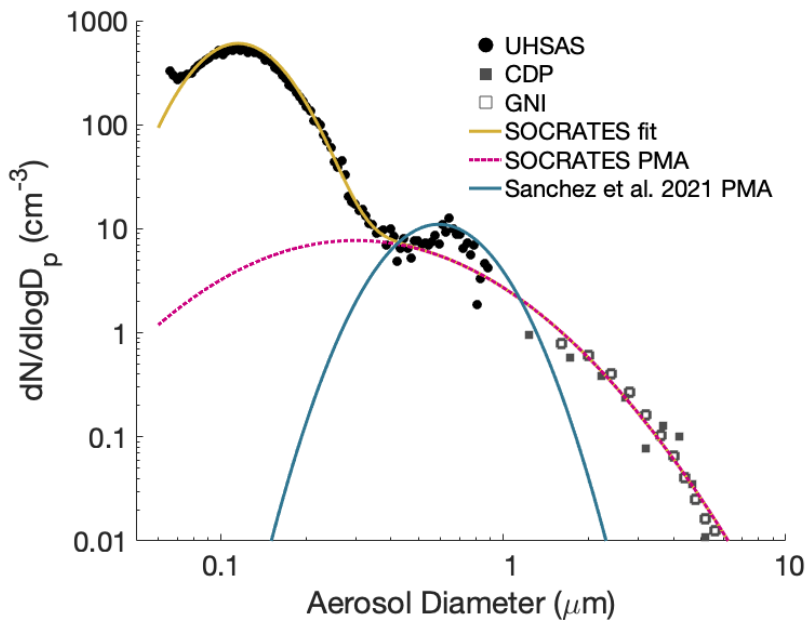


Figure 2. SOCRATES RF04 merged aerosol number distribution for a 9-minute marine boundary layer pass at 165 m. UHSAS data are given by filled circles, CDP data by filled squares, and GNI data by open squares. The log-normal fit is shown in the solid gold line. The dashed magenta line is the SOCRATES PMA estimate for comparison with the average single-mode PMA fit from Sanchez et al. (2021) in solid blue.

Direct comparisons between CAPRICORN-2 and SOCRATES MBL size distributions were possible on two research flights: RF04 (Jan. 24, 2018) and RF12 (Feb. 18, 2018). Overflights were defined where the midpoint of the G-V MBL

level leg was within 30 km of the RV *Investigator* position during the same period, and two were identified where valid size distribution measurements were available from both platforms. G-V distributions represent averages of 8-10 minute level legs in the MBL (Sec.), and CAP-2 distributions are 30-min averages, as described in Sec. . Given the large speed difference between the ship and aircraft, 2-3 CAP-2 distributions were typically identified that overlapped with each G-V overpass. Lognormal fits to G-V and CAP-2 aerosol size distributions during these overpasses are shown in Fig. 3. Although the mode positions and shapes differ slightly, good agreement in number concentration is seen in both cases for sizes >0.06 μm , which is the minimum size measured by the UHSAS on the G-V. This suggests the ship-board measurements were representative for the MBL and were not unduly influenced by being close to the ocean surface. For sizes >2 μm , the CAP-2 distributions underpredict particle number, which is likely due to supermicron particle losses not captured by the calculations of inlet transmission efficiencies (Sec.), or to spatial mismatch between the ship and aircraft. Comparisons of the total number of particles, surface area, and volume from the G-V, versus those for particles <5 μm (Fig. S3a,d,g) were used to estimate particle losses unaccounted for in the CAPRICORN-2 inlet modeling. Strong linear relationships were found between particle number ($R^2=1$; Fig. S3a) and surface area ($R^2=0.96$; Fig. S3d) <5 μm and integrated quantities, and a moderate relationship was found between particle volume <5 μm and total volume ($R^2=0.37$; Fig. S3g). This exercise indicates the CAP-2 measurements are likely to have accurately captured particle number, underestimated particle surface area by $\sim 15\%$, and underestimated particle volume by $\sim 60\%$ due to poor inlet transmission of particles >5 μm . Similar trends were seen when particles with $0.5 < D < 5$ μm were correlated with $D > 0.5$ μm (Fig. S3b,e,h), and when PMA with $D < 5$ μm were correlated with total PMA (Fig. S3c,f,i). The best-fit linear relationships shown in Fig. S3 were used to correct the integrated CAP-2 number, surface area, PMA, and volume concentrations to better represent atmospheric concentrations, and these corrected concentrations are used throughout this study for integrated quantities.

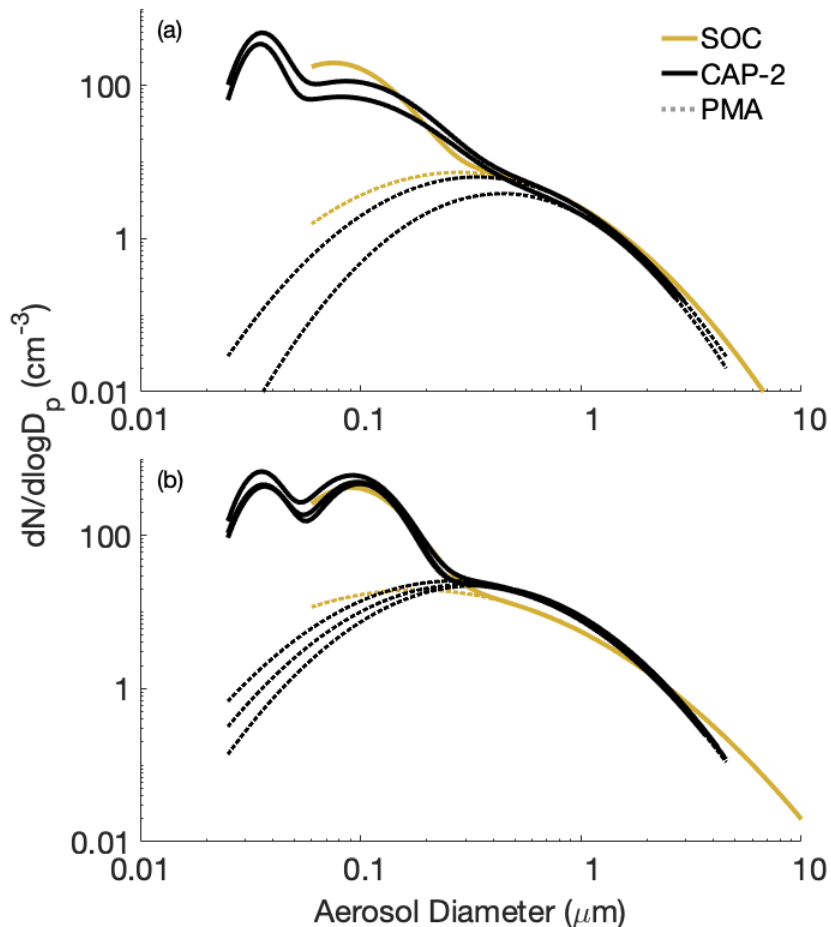


Figure 3. Comparisons of SOCRATES and CAPRICORN-2 aerosol number distributions during G-V overflights of the RV *Investigator* in the MBL. From SOCRATES flights a) RF04 and b) RF12. CAPRICORN-2 data are shown in solid black and SOCRATES MBL data in solid gold lines, with the PMA fits for both campaigns denoted by dashed lines.

Normalized histograms of integrated particle number, surface area, PMA, and volume concentrations for all CAPRICORN-2 (following additional loss corrections based on Fig. S3) and SOCRATES size distributions are shown in Fig. S4. Ranges of all quantities are similar across the two campaigns, as are the mode positions, with the best agreement for aerosol surface area (Fig. S4c). For CAP-2, the median surface area concentration is $22.9 \pm 11.1 \text{ m}^2 \text{ cm}^{-3}$, and for SOCRATES it is $25.9 \pm 12.6 \text{ m}^2 \text{ cm}^{-3}$ (\pm one standard deviation for each). CAP-2 has a larger median number concentration than SOC (Fig. S4a; CAP-2: $207 \pm 120 \text{ cm}^{-3}$; SOC: $136 \pm 80 \text{ cm}^{-3}$) and a greater fraction of distributions with

aerosol number $>400 \text{ cm}^{-3}$, which is expected due to the SOCRATES instruments being unable to capture the Aitken mode, where a significant fraction of particle number is seen in CAP-2 (Fig. 3). SOCRATES, on the other hand, has a larger median volume concentration (Fig. S4d; CAP-2: $7.0 \pm 5.3 \text{ m}^3 \text{ cm}^{-3}$; SOC: $10.3 \pm 6.6 \text{ m}^3 \text{ cm}^{-3}$) and more distributions with volume concentrations above $15 \text{ m}^3 \text{ cm}^{-3}$. In addition to differences in instrumentation, some discrepancy in aerosol volume may be due to the different regions and conditions targeted by the SOC flights compared to CAP-2. Overall, the good agreement between CAP-2 and SOC for particle surface area and volume concentrations supports the utility of the corrections presented in Fig. S3 to account for losses of $>5 \text{ m}$ particles within the CAP-2 inlet.

Fig. 4 shows total and PMA particle number, surface area, and volume concentrations as a function of wind speed for both field campaigns. Following Sanchez et al. (2021), power law relationships were fit to the PMA particle number, SA, and volume concentrations (Fig. 4b,d,f) as a function of wind speed. PMA concentrations for CAP-2 were moderately correlated with wind speed (Fig. 4b; $R^2=0.43$), as has been seen previously in the Southern Ocean (Sanchez et al., 2021) and North Atlantic (Saliba et al., 2019). PMA volume concentration is highly correlated with wind speed ($R^2=0.60$) for SOCRATES, and moderately ($R^2=0.32$) for CAP-2, which may be related to different temporal and spatial sampling rates and coverage of the G-V and RV *Investigator*, as well as instrument size restrictions that varied by campaign. The PMA number (Fig. 4b) versus wind speed relationships predicted in this study fall between those of Sanchez et al. (2021) and O’Dowd et al. (1997). Sanchez et al. (2021) only used SOCRATES UHSAS data to estimate PMA, so it is not surprising that including the coarse mode captured by the GNI and CDP (Fig. 2) during SOCRATES, and by the APS in CAP-2, increases the predicted number concentration of PMA. O’Dowd et al. (1997) used an exponential, rather than power law, model to predict PMA. It agrees well with the relationships derived in this work up to $\sim 10 \text{ m s}^{-1}$, and then rapidly diverges at higher wind speeds. In addition to the differences in functional form, the higher number concentrations predicted by O’Dowd et al. (1997) may be due to their use of particle numbers at 80% RH, rather than the dry distributions used in this work and Sanchez et al. (2021).

PMA number, surface area, and volume concentrations exhibited weak and generally insignificant correlations with latitude (Fig. S5). Nominally, SOC and CAP-2 have relationships of opposite sign between all aerosol quantities and latitude, although it should be noted the maximum latitude of the G-V was 61°S , whereas the RV *Investigator* reached the marginal ice zone at 66.5°S , in addition to there being almost 30 times fewer MBL distributions collected during SOCRATES. Sanchez et al. (2021) noted differences between the CCN latitudinal relationships for the SOC and CAP-2 campaigns, and attributed them to differences in sampling strategies and range covered, which is likely also the case here for PMA. The northern and southern transect of CAP-2 had very different PMA number concentrations north of 55°S , and highly variable

concentrations south of 60 °S, which appear to be causing the poor latitudinal correlations for this campaign. This suggests that meteorological conditions, ocean biogeochemistry, SST, or other factors are more closely related to MBL PMA concentrations over the Southern Ocean than latitude, although further study is needed. Wind speed alone explained a moderate to large proportion of PMA variance (Fig. 4), supporting this hypothesis. The impact of wind direction, which may reflect differences in warm or cold advection, have not been investigated in this study.

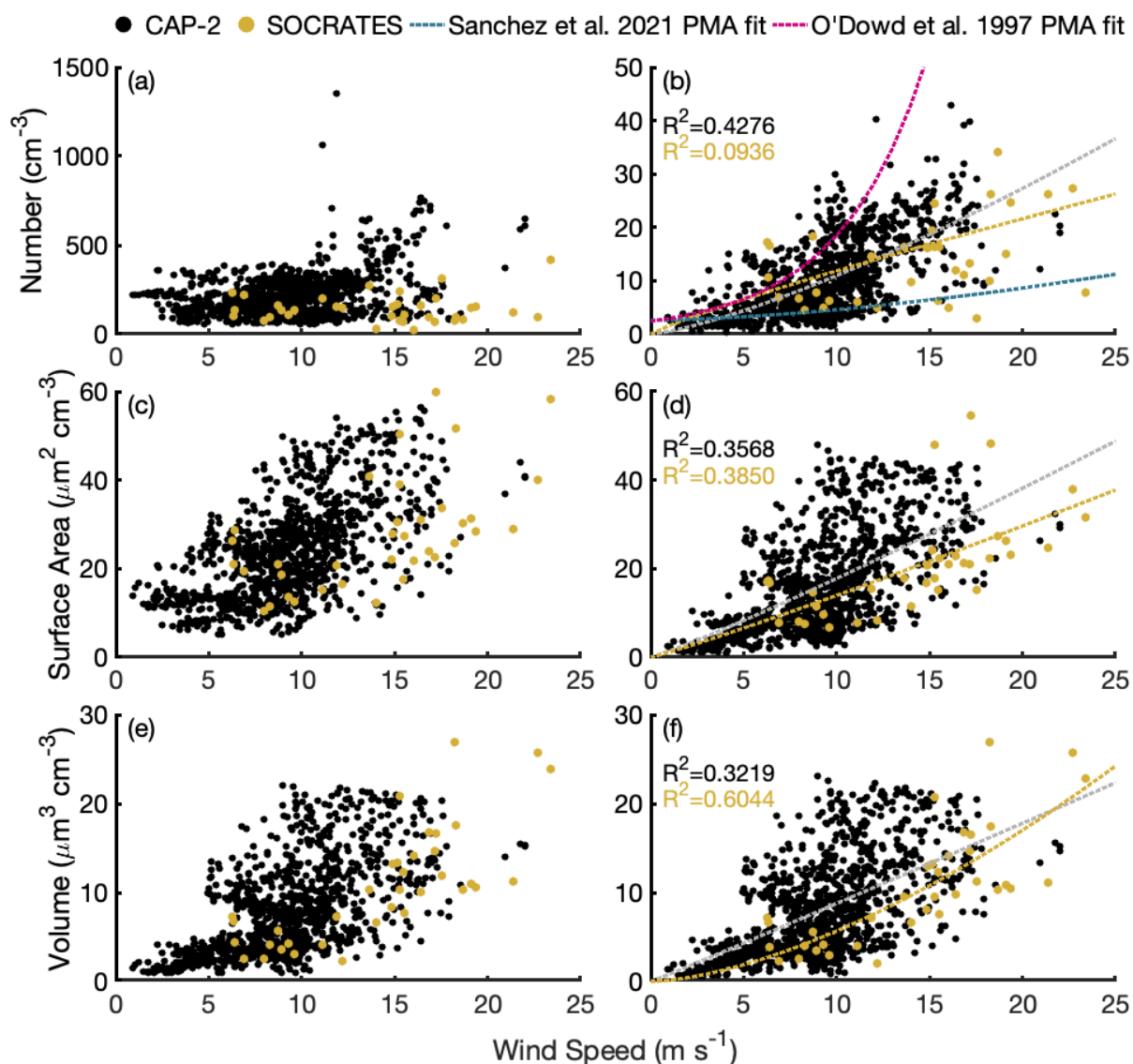


Figure 4. Particle a-b) number, c-d) surface area, and e-f) volume concentra-

tions versus wind speed. Panels a,c,e) have total concentrations and b,d,f) show PMA concentrations and best fit power law functions. CAPRICORN-2 is in black (power law fits in dashed gray), SOCRATES G-V marine boundary layer passes in gold (power law fits in dashed gold). The blue curve in (b) is the PMA fit from Sanchez et al. (2021), and the magenta curve in (b) is the PMA fit from O’Dowd et al. (1997).

1. Evaluation of D16 method for estimating marine aerosol surface area from scattering coefficients

The D16 method for retrieving dry marine aerosol surface area from bulk scattering coefficients (described in Sec.) was applied to CAP-2 using Mie calculations based on the merged aerosol size distributions. For data shown in this section only (Figs. 5-6, S6-S7), only the inlet loss corrections presented in Sec. and not the additional corrections derived from Figure S3 were applied, since the Mie calculations require size-resolved aerosol size distributions, and the corrections derived from the G-V data (Fig. S3) are only applicable to integrated quantities. This is not expected to significantly alter the results presented here, as scattering is dominated by particles smaller than 2 μm , and good agreement in particle number is seen between CAP-2 and SOCRATES below this size (Fig. 3).

Normalized frequency distributions of Ångström exponent from the CAP-2 Mie calculations are shown in Fig. S6. All three (blue/red, blue/green, green/red) distributions are bimodal, with the largest mode centered around 0-0.25, and ranging from -0.2 to ~0.8. A smaller and very broad mode occurs at larger \AA values, centered around 1.3 for all wavelength pairs. This is in very good agreement with the “clean marine” \AA frequency distribution reported by Mulcahy et al. (2009) for Northern Hemisphere marine aerosols from Mace Head, Ireland. The smaller mode centered at $\text{\AA}=1.3$ is more pronounced in the Mace Head data, which may reflect the larger bin size used in their distribution (0.2 vs 0.1 for CAP-2), in addition to differences caused by higher average wind speeds in the Southern Ocean than North Atlantic (Zheng et al., 2016), seasonal variation in sea spray production, or other factors. The CAP-2 Mie calculations are also in agreement with nephelometer measurements of Ångström exponent from coastal marine sites in NOAA’s Federated Aerosol Network (Andrews et al., 2019), as well as ship-based measurements collected near Hawaii during ACE-Asia, which reported $=0.16 \pm 0.60$ for air masses classified as marine (Carrico et al., 2003).

A comparison between aerosol surface area from the merged CAP-2 size distributions and those estimated using the D16 method applied to Mie calculations based on the same distributions is shown in Fig. 5. Very good agreement is observed for the points with low \AA values ($< \sim 0.5$), which were assigned an effective scattering efficiency of $Q=2$ based on the D16 criteria. Those points with $\text{\AA} > 1$, and assigned $Q=3$ by D16, underestimate dry aerosol surface area by a factor of 2 or more. To explore the reason for this discrepancy, average

aerosol scattering efficiency was calculated for each size distribution using Eq. 4, by replacing SA_{scat} with the measured dry aerosol surface area and solving for Q . The results for each wavelength pair are shown in Fig. 6a as a function of the Mie-calculated Ångström exponent. For the majority of the points, which cluster around $\hat{a}=\pm 0.25$, $Q=2$ is a reasonable approximation, which explains the good agreement in Fig. 5 for those distributions with $\hat{a}<0.5$. However, for distributions with $\hat{a}>1$, the calculated Q varies from about 0.5-1.5, rather than the $Q=3$ that would be assigned by D16.

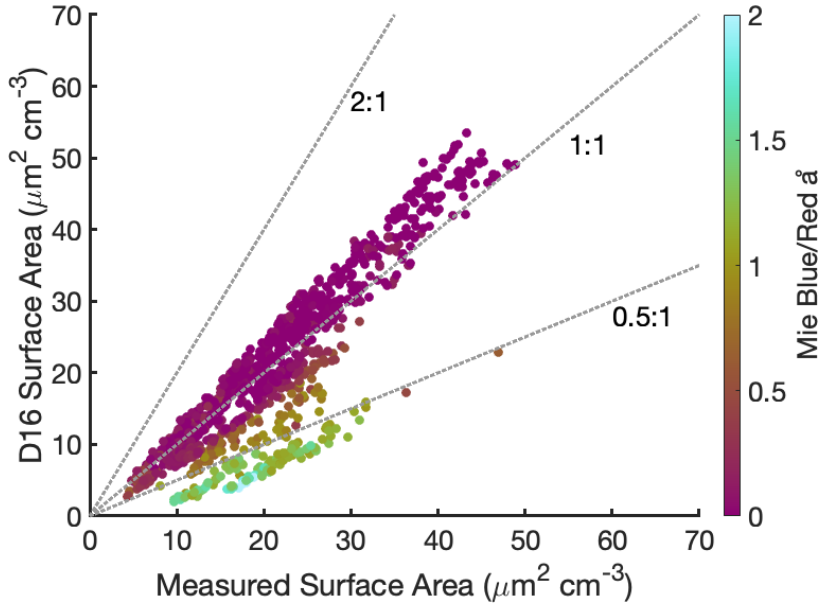


Figure 5. Correlation between total aerosol surface areas calculated by integrating the CAPRICORN-2 size distributions (x-axis) and those from the D16 method based on Mie calculations (y-axis). Symbols are colored based on the blue/red Ångström exponent from the Mie scattering calculations.

The bimodal \hat{a} distribution was investigated further in Fig. 6b-c, which again show Q calculated from Mie scattering calculations and the dry aerosol surface area against the Mie Ångström exponent, although only for the blue/red wavelength pair. Fig. 6b is colored by wind speed in 5 m s^{-1} bins, and Fig. 6c by latitude of the RV *Investigator* in 5° bins. $\hat{a}=0.8$ was selected based on Fig. S6 to separate the two modes of the Ångström exponent distribution and is indicated by the dashed lines in Fig. S6 and Fig. 6. Distributions with $\hat{a}>0.8$ primarily occur at low wind speeds and high southern latitudes. This can be seen even more clearly in Fig. S7, which shows frequency distributions of wind speed and RV *Investigator* latitude separately for aerosol distributions with blue/red $\hat{a}\leq 0.8$ and $\hat{a}>0.8$. Previous work (Saliba et al., 2021; Schmale et al., 2019; Twohy et al., 2021) have demonstrated a large proportion of CCN in the

Southern Ocean region are biogenic, and likely derive from the high chlorophyll-a waters present in the marginal ice zone, where enhanced DMS fluxes have been observed (Webb et al., 2019). DMS fluxes peak in mid-summer, the same season as CAPRICORN-2, and were estimated by Webb et al. (2019) to be sufficient to nucleate particles in the MBL near the West Antarctic Peninsula 63% of the time. Nucleation of ultrafine particles has been observed in other regions of the Antarctic coastal MBL (e.g. Humphries et al., 2015; Jokinen et al., 2018; Jung et al., 2020; Yu & Luo, 2010) in summertime, and biogenic gases are also hypothesized to contribute to condensation and the growth of particles to CCN-sizes (Twohy et al., 2021). Lower wind speeds near the Antarctic continent, in addition to the suppression of sea spray formation around the marginal ice zone (Nilsson et al., 2001) can lead to fewer large primary marine aerosol particles and lower aerosol surface area near Antarctica (Humphries et al., 2015). Based on these findings, we hypothesize that the distributions with $\text{\AA} > 0.8$ that primarily occur near the Antarctic coast are dominated by submicron biogenic particles, which control the scattering in this region due to lower PMA formation. This is supported by Humphries et al. (2021), who found the ratio of CCN to total particles increased south of 65 °S, as well as the relative contribution of sulfur to submicron aerosol mass. As a result, we have set $\text{\AA} = 0.8$ as an upper limit for defining distributions which are primarily comprised of PMA throughout this study.

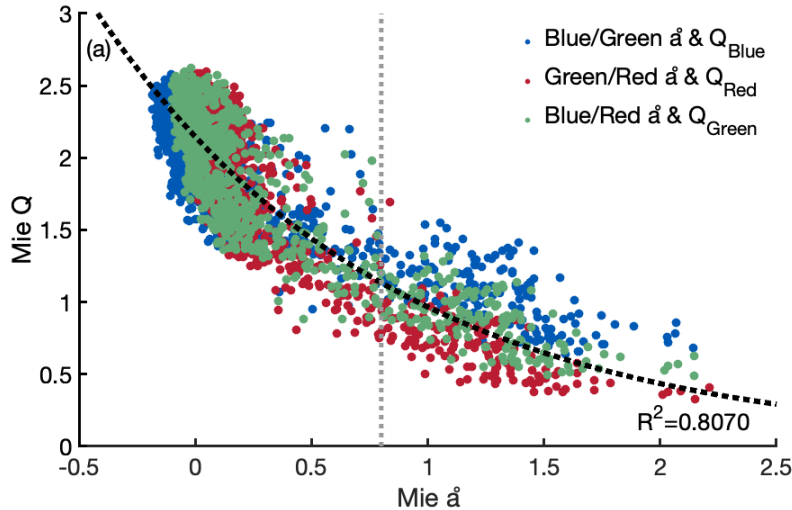


Figure 6. Relationship between Ångström exponent and average dry aerosol scattering efficiency for the CAPRICORN-2 size distributions. (a) includes \AA for all three wavelength pairs and the corresponding Q . (b) and (c) show only Q_{Green} and blue/red \AA , with symbols colored by wind speed in 5 m s^{-1} bins (b) and latitude of the RV *Investigator* in 5° bins (c). An exponential best-fit relationship between Q_{Green} and the blue/red \AA is shown on all three panels.

An exponential relationship of the form $Q = a * e^b$ was found to best describe the correlation between dry marine aerosol scattering efficiency and Ångström exponent, and the best-fit function between Q_{Green} and blue/red Å is shown on all three panels of Fig. 6. For those distributions with Å<0.8, thought to represent PMA-dominated regimes, the average Q (Q=2.00) agrees exactly with the Q=2 assigned by D16. However, Q ranges from ~1.0-2.7 for these distributions, which induces an uncertainty of ±50% when aerosol surface area is estimated using Q=2 for any distribution with Å<0.8. Distributions with Å>0.8, which would primarily be assigned Q=3 by D16, have Q ranging mostly from 0.5-1.5. Some discrepancy between the D16-assigned Q values and those calculated directly are to be expected, since the Å thresholds in D16 correspond to ambient-humidity scattering coefficients, whereas all the CAP-2 data are dry. Because of these differences, we propose that instead of the step function used by D16 to assign scattering efficiency, the exponential relationship shown in Fig. 6 ($Q_{\text{Green}} = 2.15 * e^{-0.80*}$) be used to predict Q from Å when estimating marine aerosol surface area from scattering measurements. Since this relationship was derived from Mie-calculated scattering coefficients, rather than nephelometer observations, further validation against nephelometer data will be needed.

1. Evaluation of the MA method for estimating aerosol surface area and coarse mode number concentrations using lidar extinction

The Southern Ocean is considered one of the most pristine marine regions on earth, and also has a unique meteorological environment with persistent high winds, high wave heights, and associated high concentrations of sea spray in the boundary layer (e.g. Wang et al., 2015). Therefore, as a first step, we explored whether MA’s existing marine-aerosol parameterization (Sec.) was applicable to this region. We used Level 2.0, Version 3 inversion data from the 2-year deployment of an AERONET CIMEL sun photometer during the Macquarie Island Cloud and Radiation Experiment (MICRE; Marchand, 2020; McFarquhar et al., 2021). The frequent cloudiness in the region, however, resulted in only 25 data points, and these were not representative of all seasons: 23 inversions were for data from September-December (Austral spring and early summer). Only 7 of the inversions met the MA criteria (Fig. S8). However, fourteen of the total points had Å < 0.2, suggestive of a dominant coarse mode likely associated with sea spray, despite $AOT_{500 \text{ nm}}$ as large as 0.16 (Andrews et al., 2019; Carrico et al., 2003; Mulcahy et al., 2009). In Fig. 7, we applied the MA methodology to all available MICRE data points to compute the total wet aerosol surface area and superimposed the MA correlation. MICRE data with low Å appear to be reasonably represented by the MA fit at 355 nm, although most of the points meeting the MA criteria are not. Additionally, for points near $AOT_{355 \text{ nm}} = 0.07$, it is apparent that surface area varied by a factor of 2 for the same AOT.

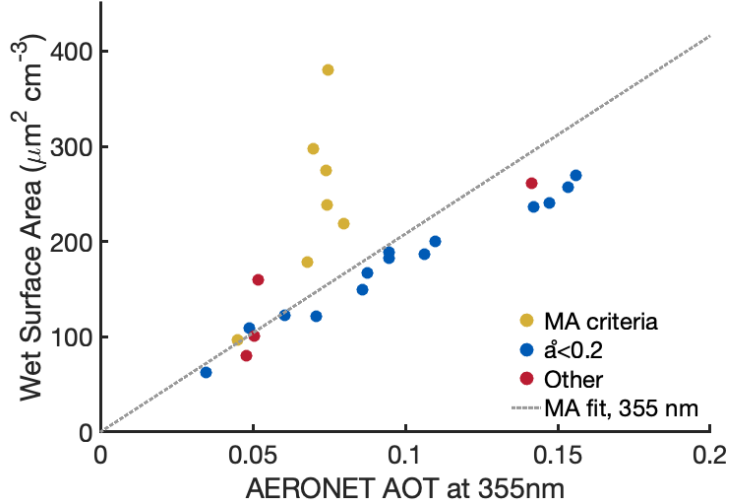


Figure 7. Column wet aerosol surface areas derived from MICRE AERONET inversions and AERONET AOT interpolated to 355 nm. The dashed line is the marine aerosol fit for 355 nm data from Mamouri and Ansmann (2016). Yellow points are those meeting the criterion applied by MA for isolating Ragged Point marine data, as described in Sec. . Dark blue points are those with $\alpha < 0.2$, expected to be dominated by coarse mode aerosol. Red points are data outside of these two classifications.

A Microtops II sun photometer was present on the RV *Investigator* as part of the AERONET Maritime Aerosol Network (MAN) and provided measurements of Ångström exponent and AOT during CAP-2 (Sec.). Although full AERONET inversions are not available from MAN measurements, the MA technique was further assessed using these open ocean Microtops data, coupled with the aerosol size distributions from CAP-2. Extinction at 355 nm, estimated from Microtops AOT using boundary layer inversion height (BLH) retrieved from radiosondes launched from the RV *Investigator* (Sec.), correlated moderately with both aerosol surface area and N_{500} (Fig. 8). AOT at 355 nm (Fig. S9) correlated more strongly with both aerosol surface area and N_{500} than did extinction, which is likely due to variability and uncertainty in estimates of BLH needed to calculate extinction. BLH of radiosondes launched during CAP-2 varied from 0.53-4.98 km, with a median of 2.07 km. The median value is consistent with the M2-M4 and C1-C2 categories discussed in Truong et al. (2020), which includes soundings from the CAP-2 campaign in addition to several others over the Southern Ocean during 2016-2018. As the CAP-2 surface area and N_{500} already represent dry values, no further adjustment to the conversion factors shown in Fig. 8 were needed to account for HGF. Notably, the conversion factors between extinction and dry aerosol surface area ($c_{s,m,microtops}/4 = 0.106 \pm 0.022 \text{ m}^2 \text{ cm}^{-3} \text{ Mm}$) and N_{500} ($c_{1000,m,microtops} = 0.0182 \pm 0.0036 \text{ cm}^{-3} \text{ Mm}$)

derived using the Microtops data are a factor of 4.9 and 2.8 smaller, respectively, than those presented in MA for marine aerosols at 355 nm.

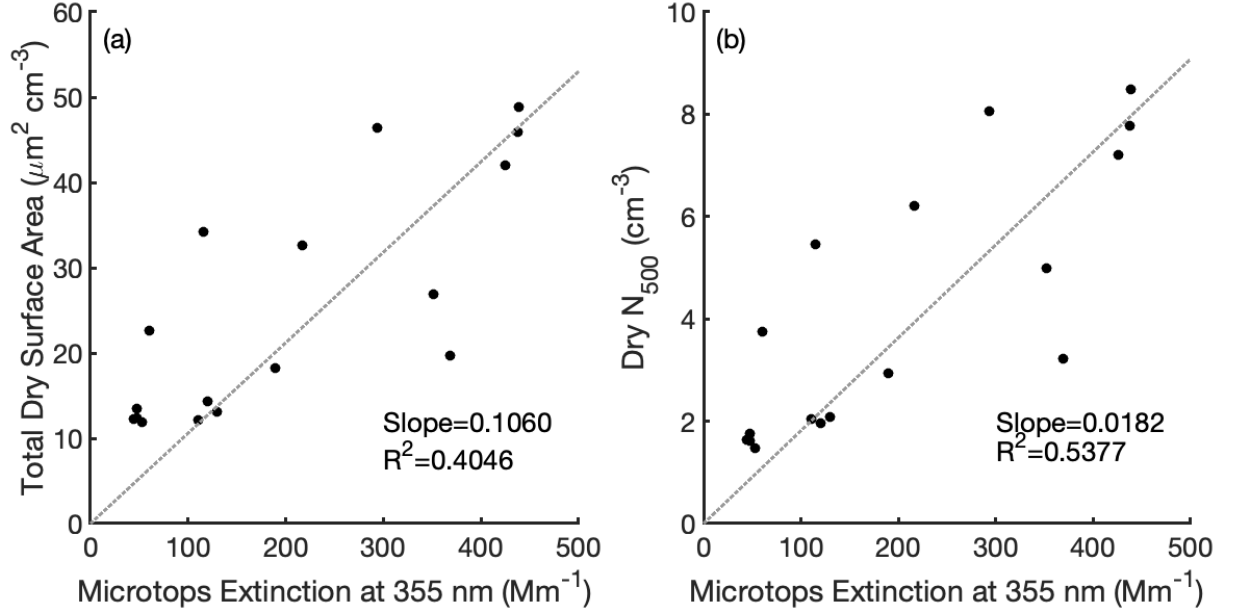


Figure 8. Correlations of extinction at 355 nm estimated from the MAN Microtops measurements with (a) total aerosol surface area and (b) N_{500} during CAPRICORN-2. Aerosol surface area and N_{500} are from merged aerosol size distributions.

Radiosondes up to 6 hours before or after a Microtops measurement were used to convert Microtops AOT to extinction, which introduces additional unaccounted-for uncertainty, since the boundary layer structure may change during that interval. To assess the influence of uncertainty in BLH, the conversion parameters were also derived from Microtops AOT_{355 nm} converted to extinction using the median CAP-2 BLH of 2.07 km instead of estimates from individual sondes. This gives an aerosol surface area parameter of $0.173 \pm 0.021 \text{ m}^2 \text{ cm}^{-3} \text{ Mm}$, and an N_{500} parameter of $0.0292 \pm 0.0042 \text{ cm}^{-3} \text{ Mm}$, which, although larger than the Microtops parameters derived from individual sondes, are still significantly smaller than the MA parameters, by factors of 3.0 and 1.7 for aerosol surface area and N_{500} , respectively. In addition to excluding data north of 47 °S (Sec.), which can be influenced by continental aerosols, all periods where the CAP-2 Mie-calculated red/blue $\tilde{a} > 0.8$ were removed (Sec.), to isolate periods where PMA is expected to be the dominant aerosol type. The remaining points have AOT_{500 nm} ranging from 0.036 - 0.127 and $\tilde{a}_{440-870 \text{ nm}}$ from 0.07 - 0.58. These agree well with other measurements of AOT and \tilde{a} for marine aerosols (Andrews et al., 2019; Carrico et al., 2003; Mulcahy et al., 2009), in addition to Mie calculations based on the CAPRICORN-2 size distributions (Sec.). It is

possible that since observations including dust are much more common in the MA marine aerosol dataset than over the Southern Ocean, their \AA ($0.25 < \text{\AA} < 0.6$) and AOT ($\text{AOT}_{500 \text{ nm}} < 0.07$) restrictions may have removed observations with significant coarse mode marine aerosol, which often has $\text{\AA} < 0.25$, and even $\text{\AA} < 0$, as well as $\text{AOT}_{500 \text{ nm}} > 0.1$ (e.g. Mulcahy et al., 2009). This could help explain the differences between their conversion parameters and those derived using the CAP-2 Microtops data.

The MA method was applied to the lidar data from CAPRICORN-2 (Sec.) using the 1) original MA marine aerosol conversion parameters at 355 nm, 2) MA parameters adjusted to account for ambient surface RH for each measurement (aerosol surface area only), and 3) new parameters derived from the CAP-2 Microtops measurements and aerosol size distributions (Fig. 8). For 2), representative HGFs for sea salt were calculated with E-AIM (Clegg et al., 1998, 2021) for each lidar profile using the average surface RH measured from the RV *Investigator* during each period, and used to scale the MA aerosol surface area conversion parameter (Sec. 2.2) to reflect the ambient boundary layer RH, rather than assuming an HGF of 2. A timeseries of aerosol surface area at 300 m estimated from lidar extinction using all three conversion parameters is shown in Fig. S10 for each clear-sky profile. When compared to the SMPS + APS observations, both MA parameters overestimate aerosol surface area for most lidar profiles, while the Microtops parameter tracks changes in dry aerosol surface area more closely. This can be seen more clearly in Fig. 9, which shows the correlation between lidar-estimated and aerosol size distribution measurements of dry aerosol surface area and N_{500} . The original MA parameters overestimate SA by a factor of ~ 3 -5, and N_{500} by ~ 1.5 -3 times. Adjusting the MA SA conversion parameter based on ambient RH typically increased the estimated dry SA and worsened the agreement by a small amount. The surface RH during CAP-2 was usually less than the 80% assumed in Mamouri and Ansmann (2016), although HGFs up to 2.6 were observed for ambient RH $\sim 90\%$ in a few cases, leading to improved correlations for those periods. The agreement was much better for both aerosol SA and N_{500} using the Microtops-derived parameters, which are distributed close to the 1:1 line in both cases. Since the calculation of extinction from lidar backscatter (Sec.) requires an assumed lidar ratio, only periods where the concurrent CAP-2 Mie-calculated red/blue $\text{\AA} < 0.8$ are shown in Fig. 9, to isolate PMA-dominated aerosol distributions (Sec. 3.2).

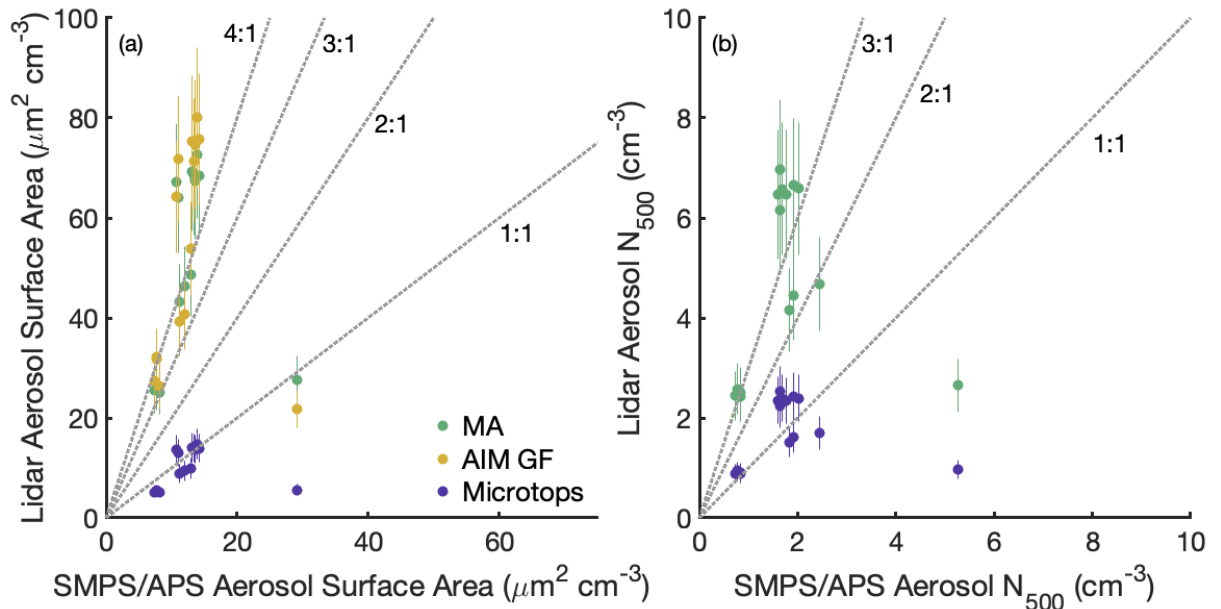


Figure 9. Comparison of CAPRICORN-2 (a) aerosol surface area and (b) N_{500} from the merged size distributions with those estimated from the lidar at 300 m using the MA method. Data using the MA parameters are shown in green, those using MA parameters adjusted for ambient RH in gold, and those using the MA method with conversion parameters derived from the CAP-2 Microtops in purple.

Both the Microtops and lidar datasets are limited to clear-sky conditions, which are infrequent in the predominantly cloudy Southern Ocean, resulting in few data points being available for both deriving the conversion parameters (Fig. 8) and testing them (Fig. 9). Additionally, the lidar profiles presented here did not cover the full range of wind speeds observed, with a median of 6.1 m s^{-1} and a maximum of 10.0 m s^{-1} . The Microtops observations covered a slightly larger range of wind speeds, with a median of 7.5 m s^{-1} and a maximum of 16.0 m s^{-1} . This effect is clear in Fig. S11, which shows normalized frequency distributions of lidar-estimated and size distribution measurements of aerosol surface area and N_{500} . The largest SA obtained from the Microtops conversion parameters is $14.8 \text{ m}^2 \text{ cm}^{-3}$, whereas for the merged size distributions it is $56.4 \text{ m}^2 \text{ cm}^{-3}$. This unfortunately limits the ability to assess the new aerosol SA and N_{500} conversion parameters across the whole range of expected conditions over the Southern Ocean, although based on this initial analysis, they perform better for this region than those presented in MA.

1. Conclusions

Measurements of aerosol size distributions from the Southern Ocean marine boundary layer were presented from the Southern Ocean Cloud Radi-

ation Aerosol Transport Experimental Study (SOCRATES) aircraft campaign and the second Clouds, Aerosols, Precipitation, Radiation and atmospheric Composition Over the southern ocean (CAPRICORN-2) ship campaign, which occurred concurrently in austral summer 2018. Close agreement was seen between size distributions measured on the G-V and RV *Investigator* during overflights for particles up to 2 μm , and corrections were presented to account for large particles not sampled efficiently by the RV *Investigator* aerosol inlet based on wing-mounted instruments from the G-V. Lognormal mode fitting was used to estimate the PMA number concentration for both campaigns, which are broadly consistent with previous measurements of sea spray aerosol in the Southern Ocean (Hartery et al., 2020; Sanchez et al., 2021) and North Atlantic (Saliba et al., 2019). Aerosol number, PMA number, surface area, and volume concentrations correlated moderately to strongly with wind speed (Fig. 4), and exhibited little or no relationship with latitude (Fig. S5).

Aerosol surface area is commonly used to parameterize ice nucleation in models, and is also important for light scattering and particle reactivity. Direct measurements are scarce over the SO, and two techniques for inferring dry marine aerosol surface area from light-scattering were evaluated here. The method presented in DeMott et al. (2016), which utilizes scattering coefficients from a three-channel nephelometer, was applied to Mie-theory calculations based on aerosol size distributions measured during CAPRICORN-2. The assignment of an effective scattering efficiency $Q=2$ for distributions with $\alpha < 1$ is a reasonable approximation (within $\pm 50\%$), although assuming $Q=3$ for distributions with $\alpha > 1$ leads to an underestimate of dry aerosol surface area by a factor of 2 or more. Instead of the step-function used to assign Q in D16, we suggest a new relationship between dry marine aerosol scattering efficiency and Ångström exponent, which explains 80% of the variance between Q and α for $-0.2 < \alpha < 2$. Additionally, we propose $\alpha=0.8$ as the cutoff between distributions dominated by PMA ($\alpha < 0.8$) and those dominated by secondary biogenic marine aerosol ($\alpha > 0.8$). The relationships derived here will need to be further assessed with ambient nephelometer data, as these were unavailable for CAP-2 or SOCRATES, and also for regions other than the Southern Ocean.

Lidar backscatter profiles have previously been shown to reproduce aerosol number and surface area concentrations in other environments (Mamouri & Ansmann, 2016), and we have evaluated their use for the Southern Ocean with CAP-2 lidar (355 nm) and aerosol measurements. The marine aerosol conversion parameters at 355 nm presented in MA were found to overestimate dry aerosol surface area by a factor of ~ 3 -5, and N_{500} by ~ 1.5 -3 times. Adjusting the MA conversion parameters based on measured RH typically worsened the agreement by a small and insignificant amount. A new set of conversion factors between ambient extinction and dry SA or N_{500} were derived from Microtops AOT measurements during CAP-2.

The Microtops parameters improve the estimation of both SA and N_{500} at 355 nm, reducing aerosol SA by 4.9 times and N_{500} by 2.8 times relative to the MA factors. However, the clear-sky lidar profiles available during CAPRICORN-2 had a maximum wind speed of 10.0 m s^{-1} , whereas 30-minute average wind speeds of $>22 \text{ m s}^{-1}$, and gusts up to 46 m s^{-1} , were observed during the campaign. Based on this initial analysis, the Microtops parameters perform better than the MA parameters for the Southern Ocean region, but they should be evaluated further over a broader range of conditions.

Data Availability

SOCRATES navigation, UHSAS, and CDP data are available from the NCAR/UCAR Earth Observing Laboratory (EOL) repository at <https://doi.org/10.5065/D6M32TM9> (UCAR/NCAR - Earth Observing Laboratory, 2019), and VCSEL RH data at <https://doi.org/10.26023/KFSD-Y8DQ-YC0D> (UCAR/NCAR - Earth Observing Laboratory, 2020). SOCRATES GNI measurements will be made available in the same database, which can be accessed here: https://data.eol.ucar.edu/master_lists/generated/socrates/. All data and samples collected during the CAPRICORN-2 voyage are made publicly available in accordance with CSIRO Marine National Facility policy. Processed data from the voyage are available at <https://doi.org/10.25919/5b71004e37a39> (CSIRO et al., 2018) following registration, and raw data are available by request (data-requests@marine.csiro.au). Quality controlled radiosonde soundings collected during CAPRICORN-2 are also available through the NCAR/UCAR EOL repository at <https://doi.org/10.5065/D69P30HG> (UCAR/NCAR - Earth Observing Laboratory, 2018). Microtops data collected during CAPRICORN-2 are available to download from the AERONET Maritime Aerosol Network website: https://aeronet.gsfc.nasa.gov/new_web/maritime_aerosol_network.html (Smirnov et al., 2009).

Acknowledgements

The authors thank Cory Wolff and Pavel Romashkin, NCAR project managers for the SOCRATES project, as well as the G-V crew, and the UCAR/NCAR-Earth Observing Laboratory for all their assistance and support. The material in the article is based upon work supported by the National Center for Atmospheric Research, which is a major facility sponsored by the National Science Foundation under Cooperative Agreement 1852977. The data collected during SOCRATES used NSF's Lower Atmosphere Observing Facilities, which are managed and operated by NCAR's Earth Observing Laboratory. We also thank the CSIRO Marine National Facility (MNF) for its support in the form of sea time on the RV Investigator, support personnel, scientific equipment, and data management during CAPRICORN-2. All data and samples acquired on the voyage are made publicly available in accordance with MNF Policy. In particular, we thank Ian McRobert (CSIRO Technical Services Officer) for assistance with the RV Investigator's electrical and data management systems and aerosol lab instrumentation during and after CAPRICORN-2, as well as Jason Ward (CSIRO

Senior Experimental Scientist) and Melita Keywood (CSIRO Senior Principal Research Scientist) for their work in maintaining aerosol equipment on the RV Investigator. We also thank Jay Mace and the CAPRICORN-2 planning team for assistance and support. This work was primarily supported by the National Science Foundation (NSF) through Grant AGS-1660486 (PJD, KAM, SMK) and by the United States Department of Energy through Grants DE-SC0018929 and DE-SC0021116 (PJD, SMK). KAM acknowledges support by an NSF Graduate Research Fellowship under Grant 006784. The contribution of SPA was supported by Australian Antarctic Science project 4292. This project also received grant funding from the Australian Government as part of the Antarctic Science Collaboration Initiative program. Any opinions, findings, and conclusions or recommendations expressed in this material are those of the author(s) and do not necessarily reflect the views of the National Science Foundation.

References

- Alexander, S. P., & Protat, A. (2018). Cloud Properties Observed From the Surface and by Satellite at the Northern Edge of the Southern Ocean. *Journal of Geophysical Research: Atmospheres*, *123*(1), 443–456. <https://doi.org/10.1002/2017JD026552>
- Alexander, S. P., & Protat, A. (2019). Vertical Profiling of Aerosols With a Combined Raman-Elastic Backscatter Lidar in the Remote Southern Ocean Marine Boundary Layer (43–66°S, 132–150°E). *Journal of Geophysical Research: Atmospheres*, *124*(22), 12107–12125. <https://doi.org/10.1029/2019JD030628>
- Andreae, M. O. (2007). Aerosols Before Pollution. *Science*, *315*(5808), 50–51. <https://doi.org/10.1126/science.1136529>
- Andrews, E., Sheridan, P. J., Ogren, J. A., Hageman, D., Jefferson, A., Wendell, J., et al. (2019). Overview of the NOAA/ESRL Federated Aerosol Network. *Bulletin of the American Meteorological Society*, *100*(1), 123–135. <https://doi.org/10.1175/BAMS-D-17-0175.1>
- Brockmann, J. E. (2011). Aerosol Transport in Sampling Lines and Inlets. In *Aerosol Measurement* (pp. 68–105). John Wiley & Sons, Ltd. <https://doi.org/10.1002/9781118001684.ch6>
- Burrows, S. M., Hoose, C., Pöschl, U., & Lawrence, M. G. (2013). Ice nuclei in marine air: biogenic particles or dust? *Atmospheric Chemistry and Physics*, *13*(1), 245–267. <https://doi.org/10.5194/acp-13-245-2013>
- Carrico, C. M., Kus, P., Rood, M. J., Quinn, P. K., & Bates, T. S. (2003). Mixtures of pollution, dust, sea salt, and volcanic aerosol during ACE-Asia: Radiative properties as a function of relative humidity. *Journal of Geophysical Research: Atmospheres*, *108*(D23). <https://doi.org/10.1029/2003JD003405>
- Carlsaw, K. S., Lee, L. A., Reddington, C. L., Pringle, K. J., Rap, A., Forster, P. M., et al. (2013). Large contribution of natural aerosols to uncertainty in indirect forcing. *Nature*, *503*(7474), 67–71. <https://doi.org/10.1038/nature12674>
- Chubb, T. H., Jensen, J. B., Siems, S. T., & Manton, M. J. (2013). In situ observations of supercooled liquid clouds over the Southern Ocean during the HIAPER Pole-to-Pole Observation campaigns. *Geophysical Research Letters*, *40*(19), 5280–5285. <https://doi.org/10.1002/grl.50986>
- Clegg, S. L., Brimblecombe, P., & Wexler, A. S. (1998). Thermodynamic Model of the System H⁺–NH₄⁺–Na⁺–SO₄²⁻

—NO₃—Cl—H₂O at 298.15 K. *The Journal of Physical Chemistry A*, 102(12), 2155–2171. <https://doi.org/10.1021/jp973043j>Clegg, S. L., Brimblecombe, P., & Wexler, A. S. (2021, May 30). E-AIM Home Page. Retrieved October 7, 2021, from <http://www.aim.env.uea.ac.uk/aim/aim.php>Corona-Núñez, R. O., Li, F., & Campo, J. E. (2020). Fires Represent an Important Source of Carbon Emissions in Mexico. *Global Biogeochemical Cycles*, 34(12), e2020GB006815. <https://doi.org/10.1029/2020GB006815>CSIRO, Marine National Facility, Rintoul, S. R., Protat, A., Bowie, A. R., Tilbrook, B., & Bodrossy, L. (2018). RV Investigator Voyage IN2018_V01 End of Voyage (EOV) Archive v4 [Data set]. CSIRO Data Collection. [Proceedings of the National Academy of Sciences, 107\(25\), 11217–11222. \[Proceedings of the National Academy of Sciences, 113\\(21\\), 5797–5803. \\[Scientific Reports, 8\\\(1\\\), 13844. \\\[Journal of Geophysical Research: Atmospheres, 125\\\\(4\\\\), e2019JD032026. \\\\[Journal of Geophysical Research: Atmospheres, 117\\\\\(D18\\\\\). \\\\\[29\\\\\]\\\\\(https://doi.org/10.1029/2012JD017800Humphries, R. S., Schofield,</p>
</div>
<div data-bbox=\\\\\)\\\\]\\\\(https://doi.org/10.1029/2019JD032026Hoose, C., & Möhler, O. \\\\(2012\\\\). Heterogeneous ice nucleation on atmospheric aerosols: a review of results from laboratory experiments. <i>Atmospheric Chemistry and Physics</i>, 12\\\\(20\\\\), 9817–9854. <a href=\\\\)\\\]\\\(https://doi.org/10.1038/s41598-018-32047-4Hamilton, D. S., Lee, L. A., Pringle, K. J., Reddington, C. L., Spracklen, D. V., & Carslaw, K. S. \\\(2014\\\). Occurrence of pristine aerosol environments on a polluted planet. <i>Proceedings of the National Academy of Sciences</i>, 111\\\(52\\\), 18466–18471. <a href=\\\)\\]\\(https://doi.org/10.1073/pnas.1514034112Fernald, F. G. \\(1984\\). Analysis of atmospheric lidar observations: some comments. <i>Applied Optics</i>, 23\\(5\\), 652–653. <a href=\\)\]\(https://doi.org/10.1073/pnas.0910818107DeMott, P. J., Prenni, A. J., McMeeking, G. R., Sullivan, R. C., Petters, M. D., Tobo, Y., et al. \(2015\). Integrating laboratory and field data to quantify the immersion freezing ice nucleation activity of mineral dust particles. <i>Atmospheric Chemistry and Physics</i>, 15\(1\), 393–409. <a href=\)](https://doi.org/10.25919/5b71004e37a39DeCarlo, P. F., Slowik, J. G., Worsnop, D. R., Davidovits, P., & Jimenez, J. L. (2004). Particle Morphology and Density Characterization by Combined Mobility and Aerodynamic Diameter Measurements. Part 1: Theory. <i>Aerosol Science and Technology</i>, 38(12), 1185–1205. <a href=)

R., Keywood, M. D., Ward, J., Pierce, J. R., Gionfriddo, C. M., et al. (2015). Boundary layer new particle formation over East Antarctic sea ice – possible Hg-driven nucleation? *Atmospheric Chemistry and Physics*, *15*(23), 13339–13364. <https://doi.org/10.5194/acp-15-13339-2015>

Humphries, R. S., McRobert, I. M., Ponsonby, W. A., Ward, J. P., Keywood, M. D., Loh, Z. M., et al. (2019). Identification of platform exhaust on the RV *Investigator*. *Atmospheric Measurement Techniques*, *12*(6), 3019–3038. <https://doi.org/10.5194/amt-12-3019-2019>

Humphries, R. S., Keywood, M. D., Gribben, S., McRobert, I. M., Ward, J. P., Selleck, P., et al. (2021). Southern Ocean latitudinal gradients of Cloud Condensation Nuclei. *Atmospheric Chemistry and Physics Discussions*, 1–35. <https://doi.org/10.5194/acp-2020-1246>

Jensen, J. B., Beaton, S. P., Stith, J. L., Schwenz, K., Colón-Robles, M., Rauber, R. M., & Gras, J. (2020). The Giant Nucleus Impactor (GNI)—A System for the Impaction and Automated Optical Sizing of Giant Aerosol Particles with Emphasis on Sea Salt. Part I: Basic Instrument and Algorithms. *Journal of Atmospheric and Oceanic Technology*, *37*(9), 1551–1569. <https://doi.org/10.1175/JTECH-D-19-0109.1>

Jokinen, T., Sipilä, M., Kontkanen, J., Vakkari, V., Tisler, P., Duplissy, E.-M., et al. (2018). Ion-induced sulfuric acid–ammonia nucleation drives particle formation in coastal Antarctica. *Science Advances*, *4*(11), eaat9744. <https://doi.org/10.1126/sciadv.aat9744>

Jung, J., Hong, S.-B., Chen, M., Hur, J., Jiao, L., Lee, Y., et al. (2020). Characteristics of methanesulfonic acid, non-sea-salt sulfate and organic carbon aerosols over the Amundsen Sea, Antarctica. *Atmospheric Chemistry and Physics*, *20*(9), 5405–5424. <https://doi.org/10.5194/acp-20-5405-2020>

Kanji, Z. A., Ladino, L. A., Wex, H., Boose, Y., Burkert-Kohn, M., Cziczo, D. J., & Krämer, M. (2017). Overview of Ice Nucleating Particles. *Meteorological Monographs*, *58*, 1.1-1.33. <https://doi.org/10.1175/AMSMONOGRAPHS-D-16-0006.1>

Kay, J. E., Bourdages, L., Miller, N. B., Morrison, A., Yettella, V., Chepfer, H., & Eaton, B. (2016). Evaluating and improving cloud phase in the Community Atmosphere Model version 5 using spaceborne lidar observations. *Journal of Geophysical Research: Atmospheres*, *121*(8), 4162–4176. <https://doi.org/10.1002/2015JD024699>

Khlystov, A., Stanier, C., & Pandis, S. N. (2004). An Algorithm for Combining Electrical Mobility and Aerodynamic Size Distributions Data when Measuring Ambient Aerosol Special Issue of Aerosol Science and Technology on Findings from the Fine Particulate Matter Supersites Program. *Aerosol Science and Technology*, *38*(sup1), 229–238. <https://doi.org/10.1080/02786820390229543>

Kiehl, J. T. (2007). Twentieth century climate model response and climate sensitivity. *Geophysical Research Letters*, *34*(22). <https://doi.org/10.1029/2007GL031383>

Kupc, A., Williamson, C., Wagner, N. L., Richardson, M., & Brock, C. A. (2018). Modification, calibration, and performance of the Ultra-High Sensitivity Aerosol Spectrometer for particle size distribution and volatility measurements during the Atmospheric Tomography Mission (ATom) airborne campaign. *Atmospheric Measurement Techniques*, *11*(1), 369–383. <https://doi.org/10.5194/amt-11-369-2018>

Lance, S., Brock, C. A., Rogers, D., & Gordon, J. A. (2010). Water droplet calibration of the Cloud Droplet Probe (CDP) and in-flight perfor-

mance in liquid, ice and mixed-phase clouds during ARCPAC. *Atmospheric Measurement Techniques*, 3(6), 1683–1706. <https://doi.org/10.5194/amt-3-1683-2010>

Lewis, E. R., & Schwartz, S. E. (2004). *Sea Salt Aerosol Production: Mechanisms, Methods, Measurements and Models—A Critical Review* (Vol. 152). Washington, DC: American Geophysical Union. Retrieved from <http://adsabs.harvard.edu/abs/2004GMS...152.3719LMace>

Mace, G. G., Protat, A., Humphries, R. S., Alexander, S. P., McRobert, I. M., Ward, J., et al. (2020). Southern Ocean Cloud Properties Derived from CAPRICORN and MARCUS Data. *Journal of Geophysical Research: Atmospheres*, e2020JD033368. <https://doi.org/10.1029/2020JD033368>

Mamouri, R.-E., & Ansmann, A. (2015). Estimated desert-dust ice nuclei profiles from polarization lidar: methodology and case studies. *Atmospheric Chemistry and Physics*, 15(6), 3463–3477. <https://doi.org/10.5194/acp-15-3463-2015>

Mamouri, R.-E., & Ansmann, A. (2016). Potential of polarization lidar to provide profiles of CCN- and INP-relevant aerosol parameters. *Atmospheric Chemistry and Physics*, 16(9), 5905–5931. <https://doi.org/10.5194/acp-16-5905-2016>

Marchand, R. (2020). *Macquarie Island Cloud and Radiation Experiment (MICRE) Final Report* (White Paper). McCluskey, C. S., Ovadnevaite, J., Rinaldi, M., Atkinson, J., Belosi, F., Ceburnis, D., et al. (2018). Marine and Terrestrial Organic Ice-Nucleating Particles in Pristine Marine to Continentally Influenced Northeast Atlantic Air Masses. *Journal of Geophysical Research: Atmospheres*, 123(11), 6196–6212. <https://doi.org/10.1029/2017JD028033>

McCluskey, C. S., Hill, T. C. J., Humphries, R. S., Rauker, A. M., Moreau, S., Stratton, P. G., et al. (2018). Observations of Ice Nucleating Particles Over Southern Ocean Waters. *Geophysical Research Letters*, 45(21), 11,989–11,997. <https://doi.org/10.1029/2018GL079981>

McCoy, D. T., Burrows, S. M., Wood, R., Grosvenor, D. P., Elliott, S. M., Ma, P.-L., et al. (2015). Natural aerosols explain seasonal and spatial patterns of Southern Ocean cloud albedo. *Science Advances*, 1(6). <https://doi.org/10.1126/sciadv.1500157>

McFarquhar, G. M., Bretherton, C. S., Marchand, R., Protat, A., DeMott, P. J., Alexander, S. P., et al. (2021). Observations of Clouds, Aerosols, Precipitation, and Surface Radiation over the Southern Ocean: An Overview of CAPRICORN, MARCUS, MICRE, and SOCRATES. *Bulletin of the American Meteorological Society*, 102(4), E894–E928. <https://doi.org/10.1175/BAMS-D-20-0132.1>

Modini, R. L., Frossard, A. A., Ahlm, L., Russell, L. M., Corrigan, C. E., Roberts, G. C., et al. (2015). Primary marine aerosol-cloud interactions off the coast of California. *Journal of Geophysical Research: Atmospheres*, 120(9), 4282–4303. <https://doi.org/10.1002/2014JD022963>

Moore, R. H., Wiggins, E. B., Ahern, A. T., Zimmerman, S., Montgomery, L., Campuzano Jost, P., et al. (2021). Sizing response of the Ultra-High Sensitivity Aerosol Spectrometer (UHSAS) and Laser Aerosol Spectrometer (LAS) to changes in submicron aerosol composition and refractive index. *Atmospheric Measurement Techniques*, 14(6), 4517–4542. <https://doi.org/10.5194/amt-14-4517-2021>

Mulcahy, J. P., O’Dowd, C. D., & Jennings, S. G. (2009). Aerosol optical depth in clean marine and continental northeast Atlantic air. *Journal of Geophysical Research*, 114(D20), D20204. <https://doi.org/10.1029/2009JD011992>

Niemand, M., Möhler, O., Vogel, B.,

Vogel, H., Hoose, C., Connolly, P., et al. (2012). A Particle-Surface-Area-Based Parameterization of Immersion Freezing on Desert Dust Particles. *Journal of the Atmospheric Sciences*, *69*(10), 3077–3092. <https://doi.org/10.1175/JAS-D-11-0249.1>

Nilsson, E. D., Rannik, Ü., Swietlicki, E., Leck, C., Aalto, P. P., Zhou, J., & Norman, M. (2001). Turbulent aerosol fluxes over the Arctic Ocean: 2. Wind-driven sources from the sea. *Journal of Geophysical Research: Atmospheres*, *106*(D23), 32139–32154. <https://doi.org/10.1029/2000JD900747>

O’Dowd, C. D., & de Leeuw, G. (2007). Marine aerosol production: a review of the current knowledge. *Philosophical Transactions of the Royal Society A: Mathematical, Physical and Engineering Sciences*, *365*(1856), 1753–1774. <https://doi.org/10.1098/rsta.2007.2043>

O’Dowd, C. D., Smith, M. H., Consterdine, I. E., & Lowe, J. A. (1997). Marine aerosol, sea-salt, and the marine sulphur cycle: a short review. *Atmospheric Environment*, *31*(1), 73–80. [https://doi.org/10.1016/S1352-2310\(96\)00106-9](https://doi.org/10.1016/S1352-2310(96)00106-9)

Prospero, J. M., Collard, F.-X., Molinié, J., & Jeannot, A. (2014). Characterizing the annual cycle of African dust transport to the Caribbean Basin and South America and its impact on the environment and air quality. *Global Biogeochemical Cycles*, *28*(7), 757–773. <https://doi.org/10.1002/2013GB004802>

Quinn, P. K., Coffman, D. J., Kapustin, V. N., Bates, T. S., & Covert, D. S. (1998). Aerosol optical properties in the marine boundary layer during the First Aerosol Characterization Experiment (ACE 1) and the underlying chemical and physical aerosol properties. *Journal of Geophysical Research: Atmospheres*, *103*(D13), 16547–16563. <https://doi.org/10.1029/97JD02345>

Quinn, P. K., Coffman, D. J., Johnson, J. E., Upchurch, L. M., & Bates, T. S. (2017). Small fraction of marine cloud condensation nuclei made up of sea spray aerosol. *Nature Geoscience*, *10*(9), 674–679. <https://doi.org/10.1038/ngeo3003>

Saliba, G., Chen, C.-L., Lewis, S., Russell, L. M., Rivellini, L.-H., Lee, A. K. Y., et al. (2019). Factors driving the seasonal and hourly variability of sea-spray aerosol number in the North Atlantic. *Proceedings of the National Academy of Sciences*, *116*(41), 20309–20314. <https://doi.org/10.1073/pnas.1907574116>

Saliba, G., Sanchez, K. J., Russell, L. M., Twohy, C. H., Roberts, G. C., Lewis, S., et al. (2021). Organic composition of three different size ranges of aerosol particles over the Southern Ocean. *Aerosol Science and Technology*, *55*(3), 268–288. <https://doi.org/10.1080/02786826.2020.1845296>

Sanchez, K. J., Roberts, G. C., Saliba, G., Russell, L. M., Twohy, C., Reeves, J. M., et al. (2021). Measurement report: Cloud processes and the transport of biological emissions affect southern ocean particle and cloud condensation nuclei concentrations. *Atmospheric Chemistry and Physics*, *21*(5), 3427–3446. <https://doi.org/10.5194/acp-21-3427-2021>

Schmale, J., Baccarini, A., Thurnherr, I., Henning, S., Efraim, A., Regayre, L., et al. (2019). Overview of the Antarctic Circumnavigation Expedition: Study of Preindustrial-like Aerosols and Their Climate Effects (ACE-SPACE). *Bulletin of the American Meteorological Society*, *100*(11), 2260–2283. <https://doi.org/10.1175/BAMS-D-18-0187.1>

Seinfeld, J. H., & Pandis, S. N. (2016). *Atmospheric Chemistry and Physics: From Air Pollution to Climate Change*. John Wiley & Sons.

Smirnov, A., Holben, B. N., Slutsker, I., Giles, D. M., McClain, C. R., Eck, T. F., et al. (2009). Maritime Aerosol Network as

a component of Aerosol Robotic Network. *Journal of Geophysical Research: Atmospheres*, 114(D6). <https://doi.org/10.1029/2008JD011257>SouthWest Sciences, I. (SWS), & UCAR/NCAR-Earth Observing Laboratory. (2008). Vertical Cavity Surface-Emitting Laser (VCSEL) Hygrometer. *UCAR/NCAR - Earth Observing Laboratory*. <https://doi.org/10.5065/D6PV6HDM>Strapp, J. W., Leitch, W. R., & Liu, P. S. K. (1992). Hydrated and Dried Aerosol-Size-Distribution Measurements from the Particle Measuring Systems FSSP-300 Probe and the Deiced PCASP-100X Probe. *Journal of Atmospheric and Oceanic Technology*, 9(5), 548–555. [https://doi.org/10.1175/1520-0426\(1992\)009<0548:HADASD>2.0.CO;2](https://doi.org/10.1175/1520-0426(1992)009<0548:HADASD>2.0.CO;2)Tang, I. N., Tridico, A. C., & Fung, K. H. (1997). Thermodynamic and optical properties of sea salt aerosols. *Journal of Geophysical Research: Atmospheres*, 102(D19), 23269–23275. <https://doi.org/10.1029/97JD01806>Truong, S. C. H., Huang, Y., Lang, F., Messmer, M., Simmonds, I., Siems, S. T., & Manton, M. J. (2020). A Climatology of the Marine Atmospheric Boundary Layer Over the Southern Ocean From Four Field Campaigns During 2016–2018. *Journal of Geophysical Research: Atmospheres*, 125(20), e2020JD033214. <https://doi.org/10.1029/2020JD033214>Twohy, C. H., DeMott, P. J., Russell, L. M., Toohey, D. W., Rainwater, B., Geiss, R., et al. (2021). Cloud-Nucleating Particles over the Southern Ocean in a Changing Climate. *Earth's Future*, in Review. UCAR/NCAR - Earth Observing Laboratory. (2005). *NSF/NCAR GV HIAPER Aircraft*. <https://doi.org/10.5065/D6DR2SJP>. UCAR/NCAR - Earth Observing Laboratory. (2018). UCAR/NCAR – Earth Observing Laboratory: NCAR/EOL ISS Radiosonde Data Version 1.0 [Data set]. <https://doi.org/10.5065/D69P30HG>. UCAR/NCAR - Earth Observing Laboratory. (2019). UCAR/NCAR – Earth Observing Laboratory: Low Rate (LRT -1 sps) Navigation, State Parameter, and Microphysics Flight-Level Data, Version 1.3 [Data set]. <https://doi.org/10.5065/D6M32TM9>. UCAR/NCAR - Earth Observing Laboratory. (2020). UCAR/NCAR – Earth Observing Laboratory: VCSEL 1Hz Water Vapor Data Version 1.0 [Data set]. <https://doi.org/10.26023/KFSD-Y8DQ-YC0D>Ullrich, R., Hoose, C., Möhler, O., Niemand, M., Wagner, R., Höhler, K., et al. (2017). A New Ice Nucleation Active Site Parameterization for Desert Dust and Soot. *Journal of the Atmospheric Sciences*, 74(3), 699–717. <https://doi.org/10.1175/JAS-D-16-0074.1>Vergara-Temprado, J., Murray, B. J., Wilson, T. W., O’Sullivan, D., Browse, J., Pringle, K. J., et al. (2017). Contribution of feldspar and marine organic aerosols to global ice nucleating particle concentrations. *Atmospheric Chemistry and Physics*, 17(5), 3637–3658. <https://doi.org/10.5194/acp-17-3637-2017>Vömel, H., & Brown, W. (2018). *SOCRATES -2018 Radiosonde Data Quality Report*, UCAR/NCAR - Earth Observing Laboratory. <https://doi.org/10.5065/D69P30HG>. Wang, Z., Siems, S. T., Belusic, D., Manton, M. J., & Huang, Y. (2015). A Climatology of the Precipitation over the Southern Ocean as Observed at Macquarie Island. *Journal of Applied Meteorology and Climatology*, 54(12), 2321–2337. <https://doi.org/10.1175/JAMC-D-14-0211.1>Webb, A. L., van Leeuwe, M. A., den Os, D., Meredith, M. P., J. Venables, H., & Stefels, J. (2019). Extreme spikes in DMS flux double

estimates of biogenic sulfur export from the Antarctic coastal zone to the atmosphere. *Scientific Reports*, *9*(1), 2233. <https://doi.org/10.1038/s41598-019-38714-4> von der Weiden, S.-L., Drewnick, F., & Borrmann, S. (2009). Particle Loss Calculator – a new software tool for the assessment of the performance of aerosol inlet systems. *Atmospheric Measurement Techniques*, *2*(2), 479–494. <https://doi.org/10.5194/amt-2-479-2009> Yu, F., & Luo, G. (2010). Oceanic Dimethyl Sulfide Emission and New Particle Formation around the Coast of Antarctica: A Modeling Study of Seasonal Variations and Comparison with Measurements. *Atmosphere*, *1*(1), 34–50. <https://doi.org/10.3390/atmos1010034> Zheng, C. W., Pan, J., & Li, C. Y. (2016). Global oceanic wind speed trends. *Ocean & Coastal Management*, *129*, 15–24. <https://doi.org/10.1016/j.ocecoaman.2016.05.001> Zieger, P., Väisänen, O., Corbin, J. C., Partridge, D. G., Bastelberger, S., Mousavi-Fard, M., et al. (2017). Revising the hygroscopicity of inorganic sea salt particles. *Nature Communications*, *8*(1), 15883. <https://doi.org/10.1038/ncomms15883> Zondlo, M. A., Paige, M. E., Massick, S. M., & Silver, J. A. (2010). Vertical cavity laser hygrometer for the National Science Foundation Gulfstream-V aircraft. *Journal of Geophysical Research: Atmospheres*, *115*(D20). <https://doi.org/10.1029/2010JD014445>